Commun. Comput. Phys.
doi: 10.4208/cicp.270515.010216a

Vol. **20**, No. 3, pp. 773-810
September 2016

Finite Element Algorithm for Dynamic Thermoelasticity Coupling Problems and Application to Transient Response of Structure with Strong Aerothermodynamic Environment

Zhihui Li[1,2,*], Qiang Ma[1,2] and Junzhi Cui[3]

[1] *Hypervelocity Aerodynamics Institute, China Aerodynamics Research and Development Center, P.O. Box 211, Mianyang 621000, China.*
[2] *National Laboratory for Computational Fluid Dynamics, BUAA, No.37 Xueyuan Road, Beijing 100191, China.*
[3] *LSEC, ICMSEC, The Academy of Mathematics and Systems Science, CAS, Beijing 100190, China.*

Received 27 May 2015; Accepted (in revised version) 1 February 2016

Abstract. As an exploratory study for structural deformation and thermodynamic response induced by spacecraft reentry aerodynamic force and thermal environment, a finite element algorithm is presented on the basis of the classic Fourier heat conductive law to simulate the dynamic thermoelasticity coupling performance of the material. The Newmark method and Crank-Nicolson scheme are utilized to discretize the dynamic thermoelasticity equation and heat conductive equation in the time domain, respectively, and the unconditionally stable implicit algorithm is constructed. Four types of finite-element computing schemes are devised and discussed to solve the thermodynamic coupling equation, all of which are implemented and compared in the computational examples including the one-dimensional transient heat conduction in considering and not considering the vibration, the transient heat flow for the infinite cylinder, and the dynamic coupling thermoelasticity around re-entry flat plate from hypersonic aerothermodynamic environment. The computational results show that the transient responses of temperature and displacement field generate lag phenomenon in case of considering the deformation effect on temperature field. Propagation, rebounding, attenuation and stabilized phenomena of elastic wave are also observed by the finite-element calculation of thermodynamic coupling problem considering vibration and damping, and the oscillation of the temperature field is simultaneously induced. As a result, the computational method and its application research platform have been founded to solve the transient thermodynamic coupling response problem of the structure in strong aerodynamic heating and force environment. By comparing various coupling calculations, it is demonstrated that the present algorithm could give a correct and reliable description of transient thermodynamic responses of

*Corresponding author. *Email addresses:* zhli0097@x263.net (Z. Li), maqiang@lsec.cc.ac.cn (Q. Ma), cjz@lsec.cc.ac.cn (J. Cui)

 ©2016 Global-Science Press

https://doi.org/10.4208/cicp.270515.010216a Published online by Cambridge University Press

structure, the rationality of the sequentially coupling method in engineering calculation is discussed, and the bending deformation mechanism produced by the thermodynamic coupling response from windward and leeward sides of flying body is revealed, which lays the foundation in developing the numerical method to solve material internal temperature distribution, structural deformation, and thermal damage induced by spacecraft dynamic thermoelasticity coupling response under uncontrolled reentry aerothermodynamic condition.

AMS subject classifications: 65Y10, 65Z05, 74S05, 76K99, 80A10

Key words: Dynamic thermoelasticity, finite element algorithm, Newmark method, Crank-Nicolson scheme, fluid-structure interaction, structural deformation.

1 Introduction

Large-scale spacecraft in orbit will face the problems of de-orbiting in fall around the end of life, and disintegrate because they suffer tremendous aerodynamic/thermal environment and overloads [1–5] during reentering back to the earth. The high-temperature thermo-chemical non-equilibrium gas flows produced by spacecraft re-entering dense atmospheric surrounding will create cumulative effect of ablative pyrolysis, and metal truss softening and melting. Under this circumstance, hypersonic aerothermodynamic problems need to be solved and meanwhile various fluid-structure interaction approaches are studied [6–8]. The high-temperature induced problems also require the analysis of the materials' phase transition and nonlinear behavior of structural response [9–15]. As a preliminary research for above issues, there will be practical significance [16, 17] to develop the dynamic thermal coupling finite-element algorithm [18] in analyzing and investigating integrated thermo-mechanical response of material structure under strong aerothermodynamic surrounding. A nonlinear finite-element method needs to be developed to study the softening/deforming and melting/failing behavior during spacecraft' reentry of uncontrolled state, and finally a fluid-thermal-solid integrated coupling numerical algorithm needs to be constructed, which has been being a challenge problem to be solved.

In engineering problems, the determination of thermal stresses is usually carried out in two steps. First, the temperature distribution is obtained from the Fourier's heat-conduction equation, the stresses are then calculated by the equations of elastostatics, including the temperature terms in the stress-strain relations. This procedure omits two important effects – the effect on the distribution of temperature as a result of the straining of the body, and the dynamic effects resulting from the inertia forces. When the material is subjected to the strong aerodynamic force and rapid aerodynamic heating, its deformation will significantly affect the temperature distribution in the interior of the material. The thermal-induced vibration should also not be neglected, and in some extreme condition, thermal shock interaction for instance, the heat propagation is to be viewed as a

https://doi.org/10.4208/cicp.270515.010216a Published online by Cambridge University Press

wave phenomenon rather than a diffusion phenomenon and this wavelike thermal disturbance is referred to as the second sound [19], then the governing equation becomes as hyperbolic-type. Combined with the dynamic thermoelasticity equation, both the temperature and structural stress fields manifest itself with complex wave behaviors, which should need a unified consideration and analysis to the coupled system of heat transfer, deformation and stresses on material and structure [20,21] so as to reflect the real physical and mechanical problem.

On the other hand, the theoretical analysis and numerical simulation for the dynamic linear and nonlinear thermoelastic performances of the materials under rigorous heat surrounding have been being an active researching area, which involves from the classical uncouple and coupled dynamic thermoelasticity to the general thermoelasticity problems based on the Lord-Shulman's and/or Green-Lindsay's theorems [22–25]. Carter and Booker [26] considered the dynamic coupled thermoelasticity problem involving structural distortion and without the inertia force terms in heat conductive equation, and discussed the application to geomechanics engineering. Prevost and Tao [27] proposed an explicit-implicit finite element method to simulate the dynamic coupled thermoelasticity problems with two relaxation times. Sherief and Anwar [28] studied the generalized thermoelasticity for an infinitely long circular cylinder composed of two different materials. Yang and Chen [29] considered the thermodynamic coupling problem near to static state with one relaxation time for the infinitely long composite cylinder, and used both the Laplace transform and the Inverse Laplace transform in the practical computation. Osamah and Abdulateef [30] investigated the thermal stress distribution in laser spot welding process. Alashti et al. [31] studied the asymmetric thermoelastic behavior for a functionally gradient rotating cylindrical shell. Ženíšek [32] studied the coupled thermoelasticity problem and made a finite-element analysis to the consolidation model of clay. Hosseini [33] made a coupled thermoelasticity finite-element simulation in the one-dimensional radial direction for functionally gradient thick hollow cylinders without the damping effect. Strunin et al. [34] considered the propagation of thermoelasticity waves in the hyperbolic thermodynamic coupling model with thermal relaxation time in the infinite rod. Ibrahim et al. [35] developed the finite-element method for the generalized thermoelasticity model also with relaxation time. Serra and Bonaldi [36] established the finite-element formulation for the fully coupled thermoelasticity problem with damping. Lutz et al. [37] presented a finite-element model for the large-scale composite space structures, and investigated its thermoelastic response under thermal load. Comprehensive analysis brings out such a question that how the computable model for dynamic thermoelasticity coupling response is set up and aimed at complex 2D and 3D structures.

In this work as the first attempt, we develop a finite element algorithm for the dynamic thermoelasticity coupling problem of materials involved in hypersonic reentry aerothermodynamic environment based on the classic Fourier heat conductive law, in which the Newmark implicit scheme is employed to discretize the dynamic thermoelasticity equation and the Crank-Nicolson scheme is used to solve the heat-conduction equation with straining coupling term. Thus the temperature increment, displacement, veloc-

https://doi.org/10.4208/cicp.270515.010216a Published online by Cambridge University Press

ity and acceleration are obtained within the same time step. The efficiency and accuracy are tested by a classic problem with analytical solutions and the bidirectional lag effect [29] on both the stress and temperature distributions are also observed. The elastic wave occurs after considering the inertia force in the coupled model. Finally we discussed the application for the simulation of fluid-structure interaction under strong aerothermodynamics environment by using the computed quantities of hypersonic aerothermodynamics coming from the gas-kinetic unified algorithm (GKUA) [38–42] for solving the Boltzmann model equation as boundary conditions for the coupled dynamic thermoelastic problem. The uniqueness and novelty of the work lies in the computable model and application of the coupling thermoelasticity (CTE) to hypersonic aerothermodynamic transient problems using fluid-structure interaction loads computed by the GKUA. The dynamic thermoelasticity coupling response behaviors including material internal temperature distribution, structural deformation, and thermal damage are simulated in real time by applying the CTE+GKUA in the field of reentering hypersonic aerothermodynamics. The remaining of this paper is organized as follows: The dynamic coupled thermoelasticity equations are introduced and the weak form is derived in Section 2. The finite-element analysis is discussed and the corresponding algorithm is proposed in Section 3. Several numerical examples are presented in Section 4, followed by conclusions and the expectation of the future work in Section 5.

2 Governing equations of dynamic thermoelasticity coupling problem

2.1 Dynamic equation of thermoelasticity

In the three-dimensional domain $\Omega \subset \mathbb{R}^3$, the dynamic thermoelasticity equation [18, 24, 25] is expressed as follows

$$\rho\frac{\partial^2 u_i}{\partial t^2}+\tau\frac{\partial u_i}{\partial t}-\frac{\partial}{\partial x_j}\left(C_{ijkl}\frac{\partial u_k}{\partial x_j}\right)+\frac{\partial}{\partial x_j}(\beta_{ij}\theta)=f_i, \tag{2.1}$$

where $\mathbf{u}=[u_1 \quad u_2 \quad u_3]^T$ is the displacement vector, $\mathbf{f}=[f_1 \quad f_2 \quad f_3]^T$ is the volume force and the superscript T denotes transposition. ρ is the density, τ is the damping coefficient and C_{ijkl} is the 4-order elasticity tensor. For homogeneous and isotropic materials, C_{ijkl} is written as

$$C_{ijkl}=\lambda\delta_{ij}\delta_{kl}+G(\delta_{ik}\delta_{jl}+\delta_{il}\delta_{jk}). \tag{2.2}$$

Here, δ_{ij} is the Kronecker symbol, λ and G are the Lamé constants, expressed by the Young's modulus E and the Possion's ration ν as

$$\lambda=\frac{E\nu}{(1+\nu)(1-2\nu)}, \quad G=\frac{E}{2(1+\nu)}. \tag{2.3}$$

https://doi.org/10.4208/cicp.270515.010216a Published online by Cambridge University Press

$\theta = T - T_0$ is the temperature increment with T and T_0 denoting the absolute temperature and reference temperature respectively and β_{ij} is the thermo-stress module,

$$\beta_{ij} = C_{ijkl}\alpha_{kl}, \tag{2.4}$$

where α_{kl} is the thermal expansion coefficient. For homogeneous and isotropic materials, $\alpha_{kl} = \alpha_0\delta_{kl}$, α_0 is the thermal expansion constant, and then β_{ij} can be written as

$$\beta_{ij} = 3\dot{\gamma}\alpha_0\delta_{ij}, \tag{2.5}$$

here $\dot{\gamma} = \frac{E}{3(1-2\nu)}$ is the bulk modulus, which means that the increment or decrement of the temperature leads to the expansion or contraction of the body, effecting the stress distribution of the structure. The elastic strain ε_{ij} is

$$\varepsilon_{ij} = \frac{1}{2}\left(\frac{\partial u_i}{\partial x_j} + \frac{\partial u_j}{\partial x_i}\right) \tag{2.6}$$

and the stress tensor σ_{ij}

$$\sigma_{ij} = C_{ijkl}\varepsilon_{kl} - \beta_{ij}\theta. \tag{2.7}$$

2.2 Transient heat conductive equation

Considering the deforming influence on the temperature field, the heat conductive equation is expressed as follows

$$\rho c\frac{\partial\theta}{\partial t} + T_0\beta_{ij}\frac{\partial}{\partial t}\left(\frac{\partial u_i}{\partial x_j}\right) - \frac{\partial}{\partial x_j}\left(k_{ij}\frac{\partial\theta}{\partial x_i}\right) = H. \tag{2.8}$$

Here, c is the specific heat, k_{ij} denotes the 2-order conductivity tensor and H is the heat source. Considering also homogeneous and isotropic materials, from the expression (2.5) of β_{ij}, the second term of Eq. (2.8) can be denoted by

$$T_0\beta_{ij}\frac{\partial}{\partial t}\left(\frac{\partial u_i}{\partial x_j}\right) = T_0\frac{E\alpha_0}{1-2\nu}\frac{\partial\varepsilon_{ii}}{\partial t}, \tag{2.9}$$

in which ε_{ii} is the volumetric strain, Eq. (2.9) illustrates that the change rate of the volumetric strain is the positive correlation with the temperature field.

2.3 Initial and boundary conditions

For the dynamic thermoelasticity equation (2.1), the initial condition involves the initial displacement and velocity of the domain Ω, i.e.

$$\mathbf{u}(x,0) = [\ u_1^0 \quad u_2^0 \quad u_3^0\ ]^T, \quad \frac{\partial\mathbf{u}}{\partial t}(x,0) = [\ v_1^0 \quad v_2^0 \quad v_3^0\ ]^T. \tag{2.10}$$

https://doi.org/10.4208/cicp.270515.010216a Published online by Cambridge University Press

For the heat conductive equation (2.8), as the unknown is chosen as temperature increment, the initial value is zero,

$$\theta(x,0)=0. \tag{2.11}$$

We assume the boundary $\partial\Omega$ is smooth enough in the displacement field, and consists of the prescribed boundary Γ_1 and the traction boundary Γ_2. The displacement is given on Γ_1 and generally taken as the clamped condition

$$\mathbf{u}=\mathbf{0}. \tag{2.12}$$

On Γ_2, the surface force $\mathbf{p}=[\ p_1 \quad p_2 \quad p_3\ ]^T$ is imposed and expressed as

$$\sigma_{ij}n_j=(C_{ijkl}\varepsilon_{kl}-\beta_{ij}\theta)n_j=p_i, \tag{2.13}$$

in which, $\mathbf{n}=[\ n_1 \quad n_2 \quad n_3\ ]^T$ is the unit vector outer normal to Γ_2. These two boundaries couldn't be overlapped, i.e. $\Gamma_1\bigcup\Gamma_2=\partial\Omega$, $\Gamma_1\bigcap\Gamma_2=\emptyset$.

The boundary in the temperature field can be divided into Γ_1' and Γ_2'. On Γ_1', the known increment value $\bar{\theta}$ is given by

$$\theta(x,t)=\bar{\theta}. \tag{2.14}$$

And on Γ_2', the boundary condition is related to the heat flux. By considering the flux, convection and radiation conditions, we have

$$-k_{ij}\frac{\partial\theta}{\partial x_j}n_j=q+H_c(\theta+T_0-T_{ext})+\kappa\sigma((\theta+T_0)^4-T_{ext}^4)), \tag{2.15}$$

where q is the prescribed flux value, T_{ext} the environment temperature, H_c the heat convective coefficient, κ the surface radiation emissivity of the material, and σ the Stefan-Boltzmann constant. For simplicity, only the flux boundary condition is considered

$$-k_{ij}\frac{\partial\theta}{\partial x_j}n_j=q. \tag{2.16}$$

These two boundaries can also not be overlapped, i.e., $\Gamma_1'\bigcup\Gamma_2'=\partial\Omega$, $\Gamma_1'\bigcap\Gamma_2'=\emptyset$.

2.4 The weak form of dynamic thermoelasticity coupling equations

Next, we will derive the weak form of the governing equations on dynamic thermoelasticity coupling problem by the variational principle. Introduce the functional spaces $V_{\Gamma_1}^3(\Omega)$ and $V_{\Gamma_1'}(\Omega)$ defined by

$$\begin{aligned} V_{\Gamma_1}^3(\Omega)&=\left\{\mathbf{v}=[\ v_1 \quad v_2 \quad v_2\ ]^T\middle|\ \sum_{i=1}^{3}||v_i||_{H^1(\Omega)}<\infty,\ \mathbf{v}=\mathbf{0}\ \text{ on }\ \Gamma_1\right\},\\ V_{\Gamma_1'}(\Omega)&=\left\{v\middle|\ ||v||_{H^1(\Omega)}<\infty,\ v=0\ \text{ on }\ \Gamma_1'\right\}, \end{aligned} \tag{2.17}$$

https://doi.org/10.4208/cicp.270515.010216a Published online by Cambridge University Press

where $H^1(\Omega)$ is the Sobolev space in which both the function and its derivatives are square-integrable, i.e., belong to function space $L^2(\Omega)$. The displacement $\mathbf{u}(x,t)$ is seen as a map

$$t\in[0,\overline{T}]\mapsto V_{\Gamma_1}^3(\Omega), \tag{2.18}$$

which means that for every t, $u(\cdot,t)\in V_{\Gamma_1}^3(\Omega)$. Similarly, the temperature increment $\theta(x,t)$ is also seen as a map

$$t\in[0,\overline{T}]\mapsto V_{\Gamma_1'}(\Omega) \tag{2.19}$$

and $\theta(\cdot,t)\in V_{\Gamma_1'}(\Omega)$.

For the dynamic thermoelasticity equation, multiplying (2.1) by the component of the vector test function $\tilde{\mathbf{u}}\in V_{\Gamma_1}^3(\Omega)$, respectively. Summing and integrating the resultant equations in the whole domain Ω, using the divergence theorem and incorporating with the boundary conditions (2.12), (2.13) and the property of $\tilde{\mathbf{u}}$ with $\tilde{\mathbf{u}}=\mathbf{0}$ on Γ_1, then, the weak form of Eq. (2.1) is expressed as

$$\int_\Omega \rho\frac{\partial^2 u_i}{\partial t^2}\tilde{u}_i dx+\int_\Omega \tau\frac{\partial u_i}{\partial t}\tilde{u}_i dx+\int_\Omega C_{ijkl}\frac{\partial u_k}{\partial x_l}\frac{\partial\tilde{u}_i}{\partial x_j}dx-\int_\Omega \beta_{ij}\theta\frac{\partial\tilde{u}_i}{\partial x_j}dx=\int_\Omega f_i\tilde{u}_i dx+\int_{\Gamma_2}p_i\tilde{u}_i ds. \tag{2.20}$$

By the same argument, multiplying the heat equation (2.8) by the scalar test function $\tilde{\theta}\in V_{\Gamma_1'}(\Omega)$ and integrating in the domain Ω, we have the weak form of Eq. (2.8) as

$$\int_\Omega \rho c\frac{\partial\theta}{\partial t}\tilde{\theta}dx+\int_\Omega T_0\beta_{ij}\frac{\partial^2 u_i}{\partial t\partial x_j}\tilde{\theta}dx+\int_\Omega k_{ij}\frac{\partial\theta}{\partial x_j}\frac{\partial\tilde{\theta}}{\partial x_i}dx=\int_\Omega H\tilde{\theta}dx-\int_{\Gamma_2'}q\tilde{\theta}ds. \tag{2.21}$$

In summary, for the convenience of our derivation, the weak form of the dynamic thermoelasticity coupling equations is to find $\mathbf{u}$ and θ, such that

$$\begin{cases}\int_\Omega \rho\frac{\partial^2 u_i}{\partial t^2}\tilde{u}_i dx+\int_\Omega \tau\frac{\partial u_i}{\partial t}\tilde{u}_i dx+\int_\Omega C_{ijkl}\frac{\partial u_k}{\partial x_l}\frac{\partial\tilde{u}_i}{\partial x_j}dx-\int_\Omega \beta_{ij}\theta\frac{\partial\tilde{u}_i}{\partial x_j}dx\\ \qquad=\int_\Omega f_i\tilde{u}_i dx+\int_{\Gamma_2}p_i\tilde{u}_i ds,\\ \int_\Omega \frac{\rho c}{T_0}\frac{\partial\theta}{\partial t}\tilde{\theta}dx+\int_\Omega \beta_{ij}\frac{\partial^2 u_i}{\partial t\partial x_j}\tilde{\theta}dx+\int_\Omega \frac{k_{ij}}{T_0}\frac{\partial\theta}{\partial x_j}\frac{\partial\tilde{\theta}}{\partial x_i}dx=\int_\Omega \frac{H}{T_0}\tilde{\theta}dx-\int_{\Gamma_2'}\frac{q}{T_0}\tilde{\theta}ds.\end{cases} \tag{2.22}$$

From the equations above, it is noted that the displacement $\mathbf{u}$ and temperature increment θ are dependent on each other, which have to be solved simultaneously in the finite-element method.

3 The finite element algorithm for dynamic thermoelasticity coupling problems

3.1 The space discretization of the weak form

Next we discuss the finite-element method [18,43–47] for solving the coupled weak form (2.22). For simplicity, we derive the computation scheme only for the homogeneous and

https://doi.org/10.4208/cicp.270515.010216a Published online by Cambridge University Press

isotropic materials. Discretize the domain Ω by the mesh and form the finite-element space V_h, where h denotes the mesh size, with the number of elements N_e and nodes N_v, respectively. In V_h, with the shape functions for the displacement and temperature denoted by $\mathbf{N}(x)$ and $\mathbf{X}(x)$, respectively, the interpolation functions of displacement $\mathbf{u}_h(x,t)$ and temperature $\theta_h(x,t)$ increment are,

$$\mathbf{u}_h(x,t)=\mathbf{N}(x)d(t),\quad \theta_h(x,t)=\mathbf{X}(x)\xi(t), \tag{3.1}$$

where $d(t)$ and $\xi(t)$ denote the vectors of node displacement and temperature, respectively.

The test function $\tilde{\mathbf{u}}$ and $\tilde{\theta}$ can also be represented in V_h as

$$\tilde{\mathbf{u}}_h(x,t)=\mathbf{N}(x)\tilde{d}(t),\quad \tilde{\theta}_h(x,t)=\mathbf{X}(x)\tilde{\xi}(t). \tag{3.2}$$

By denoting the first- and second-order derivatives with respect to time with the subscripts "$\cdot$" and "$\cdot\cdot$", respectively, we have

$$\frac{\partial \mathbf{u}_h}{\partial t}=\mathbf{N}(x)\dot{\mathbf{d}}(t),\quad \frac{\partial^2 \mathbf{u}_h}{\partial t^2}=\mathbf{N}(x)\ddot{\mathbf{d}}(t),\quad \frac{\partial \theta_h}{\partial t}=\mathbf{X}(x)\dot{\xi}(t). \tag{3.3}$$

The elasticity stiffness term $\int_\Omega C_{ijkl}\frac{\partial u_k}{\partial x_l}\frac{\partial \tilde{u}_i}{\partial x_j}dx$ in V_h can be formulated as

$$\tilde{d}^T(t)\Big(\int_{V_h}\mathbf{B}^T\mathbf{D}\mathbf{B}dx\Big)d(t), \tag{3.4}$$

where $\mathbf{B}(x)$ is the so-called strain matrix defined by

$$\mathbf{B}(x)=\partial^T\mathbf{N}(x), \tag{3.5}$$

with the matrix operator ∂ expressed as

$$\partial=\begin{bmatrix} \frac{\partial}{\partial x_1} & 0 & 0 & \frac{\partial}{\partial x_2} & 0 & \frac{\partial}{\partial x_3} \\ 0 & \frac{\partial}{\partial x_2} & 0 & \frac{\partial}{\partial x_1} & \frac{\partial}{\partial x_3} & 0 \\ 0 & 0 & \frac{\partial}{\partial x_3} & 0 & \frac{\partial}{\partial x_2} & \frac{\partial}{\partial x_1} \end{bmatrix}, \tag{3.6}$$

and $\mathbf{D}$ is the constitutive matrix represented by

$$D=\begin{bmatrix} \lambda+2G & \lambda & \lambda & 0 & 0 & 0 \\ \lambda & \lambda+2G & \lambda & 0 & 0 & 0 \\ \lambda & \lambda & \lambda+2G & 0 & 0 & 0 \\ 0 & 0 & 0 & G & 0 & 0 \\ 0 & 0 & 0 & 0 & G & 0 \\ 0 & 0 & 0 & 0 & 0 & G \end{bmatrix}. \tag{3.7}$$

The thermal gradient $\nabla\theta_h(x,t)$ has the form

$$\nabla\theta_h(x,t)=\mathbf{Y}(x)\xi(t), \tag{3.8}$$

https://doi.org/10.4208/cicp.270515.010216a Published online by Cambridge University Press

where $\mathbf{Y}(x)=\partial\mathbf{a}\mathbf{X}(x)$ is the gradient matrix with the vector $\mathbf{a}$ defined by

$$\mathbf{a}=[\ 1\quad 1\quad 1\quad 0\quad 0\quad 0\ ]^T. \tag{3.9}$$

For the coupling term in the dynamic thermoelasticity equation $\beta_{ij}\frac{\partial\tilde{u}_i}{\partial x_j}\theta$, taking $\theta_h(x,t)$ into Eq. (3.1), $\tilde{\mathbf{u}}(x,t)$ into Eq. (3.2) and $\beta_{ij}=\beta\delta_{ij}$, we have

$$\beta_{ij}\frac{\partial\tilde{u}_i}{\partial x_j}\theta=\tilde{d}^T(t)\beta\mathbf{B}^T\mathbf{a}\mathbf{X}\xi(t). \tag{3.10}$$

For the coupling term in the heat conductive equation

$$\beta_{ij}\frac{\partial^2 u_i}{\partial t\partial x_j}\tilde{\theta}=\tilde{\xi}^T(t)\beta\mathbf{X}^T\mathbf{a}^T\mathbf{B}\dot{\mathbf{d}}(t). \tag{3.11}$$

Substituting Eqs. (3.4), (3.10) and (3.11) into the weak form (2.22) and considering the arbitrariness of the test function $\tilde{\mathbf{u}}_h$ and $\tilde{\theta}_h$, we obtain the following space discretized equations of the weak form

$$\begin{cases}\mathbf{M}_\mathbf{u}\ddot{d}(t)+\mathbf{C}_\mathbf{u}\dot{d}(t)+\mathbf{K}_\mathbf{u}d(t)-\mathbf{L}\xi(t)=\mathbf{F}(t),\\ \mathbf{M}_\theta\dot{\xi}(t)+\mathbf{K}_\theta\xi(t)+\mathbf{L}^T\dot{d}(t)=\mathbf{G}(t).\end{cases} \tag{3.12}$$

The corresponding matrices are

$$\mathbf{M}_\mathbf{u}=\int_{V_j}\rho\mathbf{N}^T\mathbf{N}dx, \tag{3.13}$$

$$\mathbf{C}_\mathbf{u}=\int_{V_j}\tau\mathbf{N}^T\mathbf{N}dx, \tag{3.14}$$

$$\mathbf{K}_\mathbf{u}=\int_{V_j}\mathbf{B}^T\mathbf{D}\mathbf{B}dx, \tag{3.15}$$

$$\mathbf{L}=\int_{V_j}\beta\mathbf{B}^T\mathbf{a}\mathbf{X}dx, \tag{3.16}$$

$$\mathbf{M}_\theta=\int_{V_j}\frac{\rho c}{T_0}\mathbf{X}^T\mathbf{X}dx, \tag{3.17}$$

$$\mathbf{K}_\theta=\int_{V_j}\frac{k}{T_0}\mathbf{Y}^T\mathbf{Y}dx, \tag{3.18}$$

$$\mathbf{F}(t)=\int_{V_j}\mathbf{N}^T\mathbf{f}dx+\int_{\Gamma_2^h}\mathbf{N}^T\mathbf{p}ds, \tag{3.19}$$

$$\mathbf{G}(t)=\int_{V_j}\mathbf{X}^T\frac{H}{T_0}dx+\int_{(\Gamma_2')^h}\mathbf{X}^T\frac{q}{T_0}ds, \tag{3.20}$$

respectively. Here $\mathbf{M}_\mathbf{u}$ and $\mathbf{K}_\mathbf{u}$ are the $3N_v\times 3N_v$ global elastic mass and stiffness matrices, respectively, and $\mathbf{M}_\theta$ and $\mathbf{K}_\theta$ are the $N_v\times N_v$ "corrected" global heat mass and stiffness

https://doi.org/10.4208/cicp.270515.010216a Published online by Cambridge University Press

matrices because of division by T_0 . $\mathbf{C_u}$ is the $3N_v \times 3N_v$ global damping matrix and accounts for dissipation of energy. In engineering, $\mathbf{C_u}$ is often chosen as the Rayleigh damping, i.e.,

$$\mathbf{C_u} = \tau_1 \mathbf{M_u} + \tau_2 \mathbf{K_u}, \tag{3.21}$$

where τ_1 and τ_2 are the parameters that are typically determined by experiments and means that the damping is the sum of viscous and solid damping. $\mathbf{L}$ is called as the $3N_v \times N_v$ coupling matrix. Γ_2^h and $(\Gamma_2')^h$ are the discretized approximation of the boundaries Γ_2 and Γ_2' in V_h, respectively.

3.2 Newmark algorithm and Crank-Nicolson scheme

Based on the space discretization system (3.12), we then discretize the derivative terms $\ddot{d}(t)$, $\dot{d}(t)$ and $\dot{\xi}(t)$. Divide the time internal $[0,\overline{T}]$ into N equidistant sub-internals

$$0 = t_0 < t_1 < \cdots < t_N = \overline{T}, \tag{3.22}$$

with the time step $\Delta t = \overline{T}/N$, $t_n = n\Delta t$, $n = 0,1,2,\cdots,N$. The unknown at the time t_n is presented by superscript as

$$d^n = d(t_n), \quad \dot{d}^n = \dot{d}(t_n), \quad \ddot{d}^n = \ddot{d}(t_n), \quad \dot{\xi}^n = \dot{\xi}(t_n). \tag{3.23}$$

Adopting the Newmark implicit method [48, 49] to deal with the velocity and acceleration terms, we have the time stepping scheme

$$\begin{aligned}
&\Big(\frac{1}{\eta\Delta t^2}\mathbf{M_u} + \frac{\omega}{\eta\Delta t}\mathbf{C_u} + \mathbf{K_u}\Big) d^{n+1} - \mathbf{L}\xi^{n+1} \\
=&\mathbf{F}^{n+1} + \mathbf{M_u}\Big(\frac{1}{\eta\Delta t^2}d^n + \frac{1}{\eta\Delta t}\dot{d}^n + \Big(\frac{1}{2\eta} - 1\Big)\ddot{d}^n\Big) \\
&+ \mathbf{C_u}\Big(\frac{\omega}{\eta\Delta t}d^n + \Big(\frac{\omega}{\eta} - 1\Big)\dot{d}^n + \Big(\frac{\omega}{2\eta} - 1\Big)\Delta t\ddot{d}^n\Big),
\end{aligned} \tag{3.24}$$

where the parameters $0 \le \omega \le 1$, $0 \le \eta \le 1/2$, and usually when $\omega \ge 0.5$ and $\eta \ge 0.25(0.5+\omega)^2$, the scheme above is unconditionally stable.

At the initial time, $\ddot{d}^0$ is needed, which can be computed by

$$\mathbf{M_u}\ddot{d}^0 + \mathbf{C_u}\dot{d}^0 + \mathbf{K_u}d^0 - \mathbf{L}\xi^0 = \mathbf{F}^0. \tag{3.25}$$

Using the second-order Crank-Nicolson scheme [49–51] to deal with the weak form of the heat equation, we obtain

$$\Big(\mathbf{M}_\theta + \frac{\Delta t}{2}\mathbf{K}_\theta\Big)\xi^{n+1} + \mathbf{L}^T d^{n+1} = \Big(\mathbf{M}_\theta - \frac{\Delta t}{2}\mathbf{K}_\theta\Big)\xi^n + \mathbf{L}^T d^n + \frac{\Delta t}{2}(\mathbf{G}^{n+1} + \mathbf{G}^n). \tag{3.26}$$

https://doi.org/10.4208/cicp.270515.010216a Published online by Cambridge University Press

Finally, write (3.24) and (3.26) in the unified matrix form

$$\begin{aligned}
&\begin{bmatrix} \frac{1}{\eta\Delta t^2}\mathbf{M_u}+\frac{\omega}{\eta\Delta t}\mathbf{C_u}+\mathbf{K_u} & -\mathbf{L} \\ \mathbf{L}^T & \mathbf{M}_\theta+\frac{\Delta t}{2}\mathbf{K}_\theta \end{bmatrix} \begin{bmatrix} d^{n+1} \\ \xi^{n+1} \end{bmatrix} \\
=&\begin{bmatrix} \frac{1}{\eta\Delta t^2}\mathbf{M_u}+\frac{\omega}{\eta\Delta t}\mathbf{C_u} & 0 \\ \mathbf{L}^T & \mathbf{M}_\theta-\frac{\Delta t}{2}\mathbf{K}_\theta \end{bmatrix} \begin{bmatrix} d^{n} \\ \xi^{n} \end{bmatrix} \\
&+\begin{bmatrix} \mathbf{F}^{n+1}+\mathbf{M_u}(\frac{1}{\eta\Delta t}\dot{d}^n+(\frac{1}{2\eta}-1)\ddot{d}^n)+\mathbf{C_u}((\frac{\omega}{\eta}-1)\dot{d}^n+(\frac{\omega}{2\eta}-1)\Delta t\ddot{d}^n) \\ \frac{\Delta t}{2}(\mathbf{G}^{n+1}+\mathbf{G}^n) \end{bmatrix}. \qquad (3.27)
\end{aligned}$$

This is the general time stepping scheme of the dynamic coupled thermoelasticity equations, which is called as the Direct Coupling (DC) method [18, 26, 27]. According to different conditions, there are three simplified cases:

(1) Without the elastic vibration and damping, Eq. (3.27) is simplified as

$$\begin{bmatrix} \mathbf{K_u} & -\mathbf{L} \\ \mathbf{L}^T & \mathbf{M}_\theta+\frac{\Delta t}{2}\mathbf{K}_\theta \end{bmatrix} \begin{bmatrix} d^{n+1} \\ \xi^{n+1} \end{bmatrix} = \begin{bmatrix} 0 & 0 \\ \mathbf{L}^T & \mathbf{M}_\theta-\frac{\Delta t}{2}\mathbf{K}_\theta \end{bmatrix} \begin{bmatrix} d^{n} \\ \xi^{n} \end{bmatrix} + \begin{bmatrix} \mathbf{F}^{n+1} \\ \frac{\Delta t}{2}(\mathbf{G}^{n+1}+\mathbf{G}^n) \end{bmatrix}. \qquad (3.28)$$

It is a static problem for the thermoelasticity equation. If we write it in increment form, i.e.

$$d^{n+1}=d^n+\Delta d^n, \quad \xi^{n+1}=\xi^n+\Delta\xi^n, \quad \mathbf{F}^{n+1}=\mathbf{F}^n+\Delta\mathbf{F}^n, \qquad (3.29)$$

set $\mathbf{G}^n=0$ and use the fully implicit scheme for the temperature, we obtain the stepping matrix

$$\begin{bmatrix} \mathbf{K_u} & -\mathbf{L} \\ \mathbf{L}^T & \mathbf{M}_\theta+\Delta t\mathbf{K}_\theta \end{bmatrix} \begin{bmatrix} \Delta d^n \\ \Delta\xi^n \end{bmatrix} = \begin{bmatrix} \Delta\mathbf{F}^n \\ -\Delta t\mathbf{K}_\theta\xi^n \end{bmatrix}, \qquad (3.30)$$

which is the computing scheme in [26].

(2) Considering the vibration while neglecting deformation due to temperature, Eq. (3.27) is simplified and two equations are now decoupled. In the practical computation, the temperature increment can be solved separately, and the displacement field is obtained sequentially with an extra volume load from the temperature field. The two steps are, respectively,

$$\left(\mathbf{M}_\theta+\frac{\Delta t}{2}\mathbf{K}_\theta\right)\xi^{n+1}=\left(\mathbf{M}_\theta-\frac{\Delta t}{2}\mathbf{K}_\theta\right)\xi^n+\frac{\Delta t}{2}(\mathbf{G}^{n+1}+\mathbf{G}^n), \qquad (3.31)$$

$$\begin{aligned}
\left(\frac{1}{\eta\Delta t^2}\mathbf{M_u}+\frac{\omega}{\eta\Delta t}\mathbf{C_u}+\mathbf{K_u}\right)d^{n+1}=&\mathbf{F}^{n+1}+\mathbf{L}\xi^{n+1}+\mathbf{M_u}\left(\frac{1}{\eta\Delta t^2}d^n+\frac{1}{\eta\Delta t}\dot{d}^n+\left(\frac{1}{2\eta}-1\right)\ddot{d}^n\right) \\
&+\mathbf{C_u}\left(\frac{\omega}{\eta\Delta t}d^n+\left(\frac{\omega}{\eta}-1\right)\dot{d}^n+\left(\frac{\omega}{2\eta}-1\right)\Delta t\ddot{d}^n\right). \qquad (3.32)
\end{aligned}$$

It is the procedure of thermal-stress analysis in engineering, which is called as the Sequentially Coupling (SC) or Indirect Coupling method.

https://doi.org/10.4208/cicp.270515.010216a Published online by Cambridge University Press

(3) Neither vibration nor deformation due to temperature is considered, the scheme is further simplified and two equations are also decoupled, then, the practicable computation can be divided into two separate steps

$$\left(\mathbf{M}_\theta+\frac{\Delta t}{2}\mathbf{K}_\theta\right)\xi^{n+1}=\left(\mathbf{M}_\theta-\frac{\Delta t}{2}\mathbf{K}_\theta\right)\xi^{n}+\frac{\Delta t}{2}(\mathbf{G}^{n+1}+\mathbf{G}^{n}), \tag{3.33}$$

$$\mathbf{K_u}d^{n+1}=\mathbf{L}\xi^{n+1}+\mathbf{F}^{n+1}. \tag{3.34}$$

This is the often-used Sequentially Coupling method and the thermoelasticity equation also becomes static.

To sum up, we have obtained four various finite-element computation schemes for the dynamic coupled thermoelasticity problem, which are illustrated in Fig. 1. Depending on whether the coupling term is present in the heat equation, we have the DC and SC method, respectively. Each of the two methods is further divided into two cases by considering the vibration inclusively and exclusively. The four finite-element methods are different from each other, but also have some correlations denoted as the DC-Vib-Incl, DC-Vib-Excl, SC-Vib-Incl and SC-Vib-Excl, which will be discussed in one specific numerical example in Section 4.

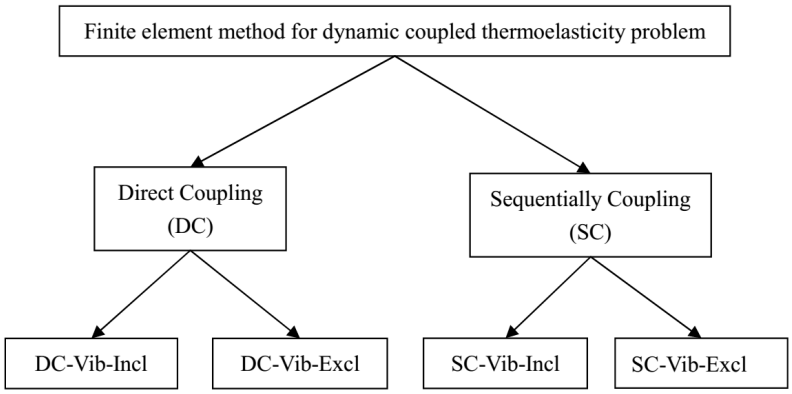


Figure 1: Illustration of the four finite-element methods for solving the dynamic coupled thermoelasticity problem.

3.3 The finite element procedure of dynamic coupled thermoelasticity problem

Here we present the computation procedure for the general DC-Vib-Incl finite element method.

1. Set the material coefficients ρ, c, E and ν (or λ and G), β(or α), τ (or τ_1, τ_2), reference temperature T_0 and Newmark parameters η, ω. Configure the domain Ω, make the space discretization and obtain the computation mesh. Set the time interval $[0,\overline{T}]$, time step number N and time step size $\Delta t=\overline{T}/N$ and take $n=0$ as the initial step.

https://doi.org/10.4208/cicp.270515.010216a Published online by Cambridge University Press

2. Compute the element matrices, assemble the global matrices $\mathbf{M_u}$, $\mathbf{C_u}$, $\mathbf{K_u}$, $\mathbf{L}$, $\mathbf{M}_\theta$ and $\mathbf{K}_\theta$, and form the following matrices

$$\begin{bmatrix} \frac{1}{\eta\Delta t^2}\mathbf{M_u}+\frac{\omega}{\eta\Delta t}\mathbf{C_u}+\mathbf{K_u} & -\mathbf{L} \\ \mathbf{L}^T & \mathbf{M}_\theta+\frac{\Delta t}{2}\mathbf{K}_\theta \end{bmatrix}, \quad \begin{bmatrix} \frac{1}{\eta\Delta t^2}\mathbf{M_u}+\frac{\omega}{\eta\Delta t}\mathbf{C_u} & 0 \\ \mathbf{L}^T & \mathbf{M}_\theta-\frac{\Delta t}{2}\mathbf{K}_\theta \end{bmatrix}. \tag{3.35}$$

Assemble the initial load vector $\mathbf{F}^0$, obtain d^0, $\dot{d}^0$ and ξ^0 from the initial condition and compute the acceleration $\ddot{d}^0$,

$$\ddot{d}^0=\mathbf{M_u}^{-1}(\mathbf{F}^0-\mathbf{K_u}d^0-\mathbf{C_u}\dot{d}^0+\mathbf{L}\xi^0). \tag{3.36}$$

3. Assemble the global load vector $\mathbf{F}^{n+1}$ and $\mathbf{G}^{n+1}$ at time step and form the load vector

$$\begin{bmatrix} \mathbf{F}^{n+1}+\mathbf{M_u}(\frac{1}{\eta\Delta t}\dot{d}^n+(\frac{1}{2\eta}-1)\ddot{d}^n)+\mathbf{C_u}((\frac{\omega}{\eta}-1)\dot{d}^n+(\frac{\omega}{2\eta}-1)\Delta t\ddot{d}^n) \\ \frac{\Delta t}{2}(\mathbf{G}^{n+1}+\mathbf{G}^n) \end{bmatrix}. \tag{3.37}$$

Apply the corresponding boundary conditions for the displacement and temperature increment, and obtain the value d^{n+1}, ξ^{n+1} at time step $n+1$.

4. Compute the velocity $\dot{d}^{n+1}$ and acceleration $\ddot{d}^{n+1}$, and obtain the heat flux q_i^{n+1}, strain ε_{ij}^{n+1} and thermal stress σ_{ij}^{n+1}, as follows

$$\begin{aligned} \ddot{d}^{n+1}&=\frac{1}{\eta\Delta t^2}(d^{n+1}-d^n)-\frac{1}{\eta\Delta t}\dot{d}^n-\left(\frac{1}{2\eta}-1\right)\ddot{d}^n, \\ \dot{d}^{n+1}&=\dot{d}^n+[(1-\omega)\ddot{d}^n+\omega\ddot{d}^{n+1}]\Delta t, \\ q_i^{n+1}&=-k_{ij}\frac{\partial\theta^{n+1}}{\partial x_j}, \\ \varepsilon_{ij}^{n+1}&=\frac{1}{2}\left(\frac{\partial u_i^{n+1}}{\partial x_j}+\frac{\partial u_j^{n+1}}{\partial x_i}\right), \\ \sigma_{ij}^{n+1}&=C_{ijkl}\varepsilon_{kl}^{n+1}-\beta_{ij}\theta^{n+1}. \end{aligned} \tag{3.38}$$

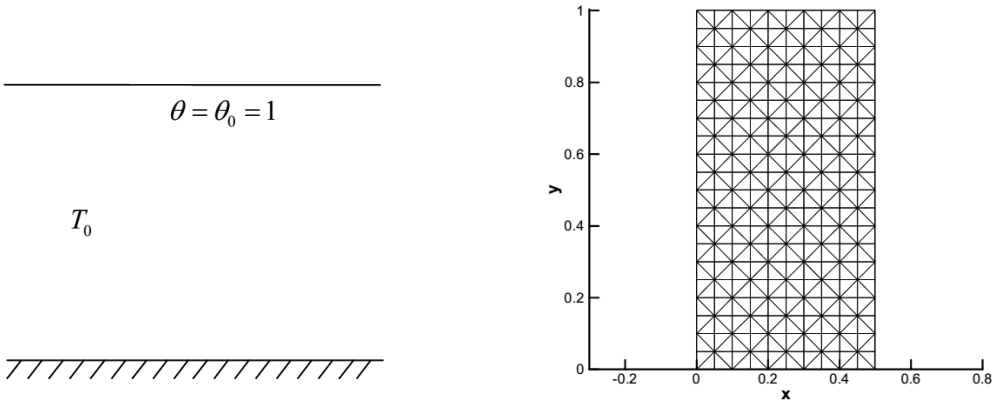
5. Set $n=n+1$, when $n>N$, finish computing, otherwise return to Step 3.

4 Numerical examples and discussion

In this section, the finite-element algorithm developed in the foregoing subsections will be used to study the transient response of structure with strong aerodynamic heating and force environment. First, we verify the method in the one-dimension transient heat conduction and the two-dimensional transient heat flow of the infinite cylinder. After that, the current method is also applied to the simulation of one-dimension transient heat flow problem considering vibration and damping effect, and the coupled thermoelastic analysis of a plate in a hypersonic re-entry flow. Here, the second-order nodal iso-parametric triangular shape functions are used to perform the finite element computations.

https://doi.org/10.4208/cicp.270515.010216a Published online by Cambridge University Press

4.1 Solving the 1D transient heat conduction problem



(a) Coupled domain of the elastic material (b) Finite element mesh of rectangle domain

Figure 2: One-dimension model for the dynamic coupled thermoelasticity problem and the computational mesh, with node number 231 and element number 400 on domain $\Omega=[0,0.5]\times[0,1]$.

The first case is about the transient heat conduction of the thermoelastic material layer with unit thickness, shown in Fig. 2(a). The layer is initially at a uniform absolute temperature T_0 throughout. For $t>0$, the temperature of the top surface ($y=1$) is maintained at $T=T_0+\theta_0$, i.e. the increment is θ_0. The bottom ($y=0$) is rigid ($\mathbf{u}=\mathbf{0}$) and insulated, there are no vibration, body force, heat source, external traction force or boundary flux. From [26], the problem has analytical solutions with the expressions of displacement $\mathbf{u}$ and temperature increment θ defined by

$$u_1=0,\quad \bar{u}_2=\frac{\beta}{s\mu M}\frac{\sinh(\mu y)}{\cosh(\mu)},\quad \bar{\theta}=\frac{\cosh(\mu y)}{\cosh(\mu)s}, \tag{4.1}$$

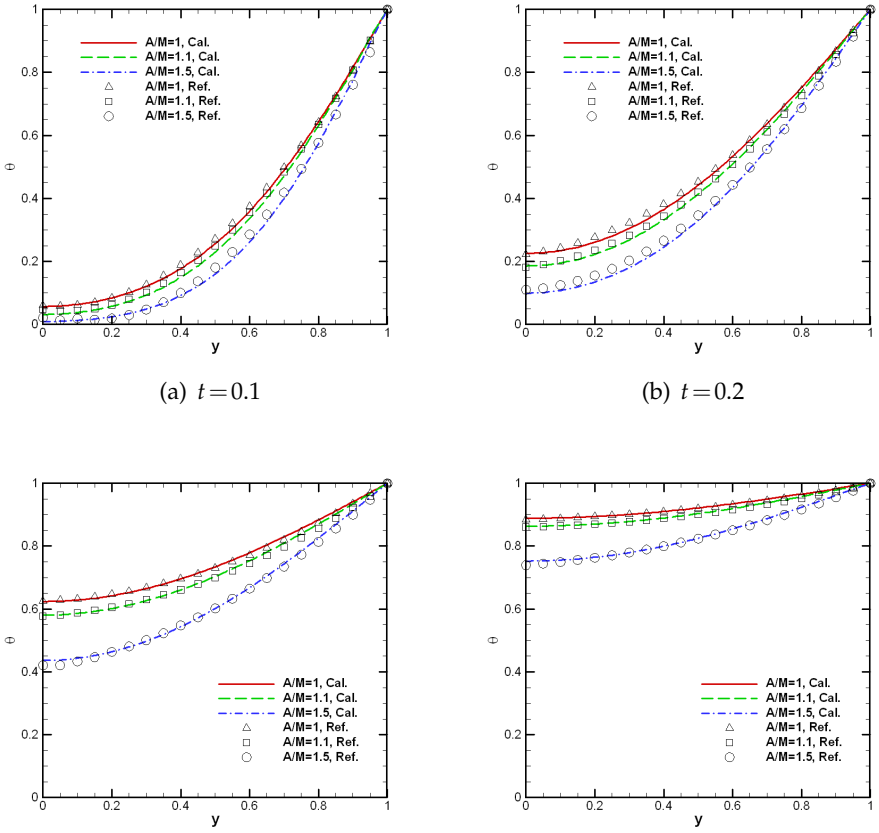
where $\bar{u}_2$ and $\bar{\theta}$ are the Laplace transforms of u_2 and θ, $\mu=\sqrt{(sA/km)}$, s is the variable of the Laplace transform, M and A are related to thermal and elastic coefficients of the material and defined by

$$M=\lambda+2G=\frac{E(1-\nu)}{(1+\nu)(1-2\nu)},\quad A=M+\frac{\beta^2T_0}{\rho c}, \tag{4.2}$$

u_2 and θ can be obtained by the inverse Laplace transform. Here, the ratio $r_c=A/M$ is used to measure the coupling degree of the two physical fields. The coupling is stronger with increasing r_c ($r_c\geq 1$), especially, $r_c=1$ means that θ is uncoupled from $\mathbf{u}$.

As for the characteristic of the domain, we use the two-dimension rectangle domain to simulate the one-dimension transient thermodynamic coupling problem, and then it is needed to solve a two-dimensional plain-strain dynamic equation. Set the domain of

https://doi.org/10.4208/cicp.270515.010216a Published online by Cambridge University Press



(a) $t=0.1$ (b) $t=0.2$

(c) $t=0.5$ (d) $t=1.0$

Figure 3: Time history of the temperature distributions along with y-direction in different coupling ratios r_c.

the material layer be $\Omega=[0,0.5]\times[0,1]$ with triangular mesh depicted in Fig. 2(b). In the problem, the length of material is infinite in x-direction and we consider displacement only along y coordinate and set the bottom boundary clamped. On the top $y=1$, the temperature increment is set to be $\theta_0=1$ and all other boundaries are insulated. Take the following non-dimensional coefficients

$$\rho=1.0,\quad c=1.0,\quad k=1.0,\quad E=2.0,\quad \nu=0.3,\quad \beta=0.05, \tag{4.3}$$

and the reference temperature T_0 is determined by the ratio r_c. As the structure vibration is not considered, the computation schemes (1) and (3) in Section 3.2 are carried out. When the uncoupled state ($r_c=1$) is concerned, the Sequentially Coupling method (SC-Vib-Excl) is used.

The temperature increment in y-direction at the time $t=0.1$, 0.2, 0.5 and 1.0 with different coupling ratios $r_c=1$, 1.1 and 1.5 are illustrated in Fig. 3(a)-(d), where the curves

https://doi.org/10.4208/cicp.270515.010216a Published online by Cambridge University Press

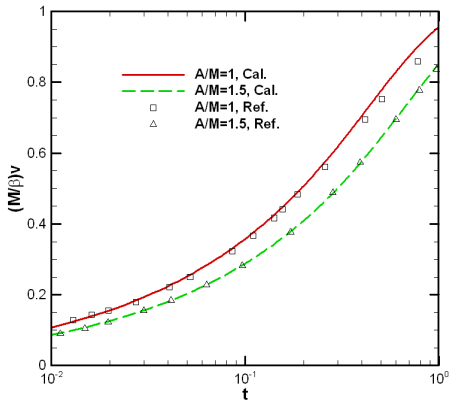


Figure 4: Time history of the thermal expansion of the outer surface for the material at $r_c=1$ and 1.5.

are the computed results in the present algorithm and the symbols denote the results from [26]. The changes of the present computed results at different time in various coupling ratios match well with both the data from [26] and the analytical solutions, which demonstrate the accuracy and reliability of the present algorithm.

To reveal the varying law of the outer surface displacement for the material induced by transient heat conduction, Fig. 4 shows the comparison of the time history of the normalized vertical displacement (lines) and the results from [26] (symbols) for the two states $r_c=1$ and 1.5 of thermodynamic coupling response. The good agreement of the two results validates the correctness of the present finite-element algorithm in computing the thermal-induced deformation. It is indicated that there is also a clear lag of the body displacement expansion in the coupled state compared with the uncoupled one, due to the lag of the temperature increasing.

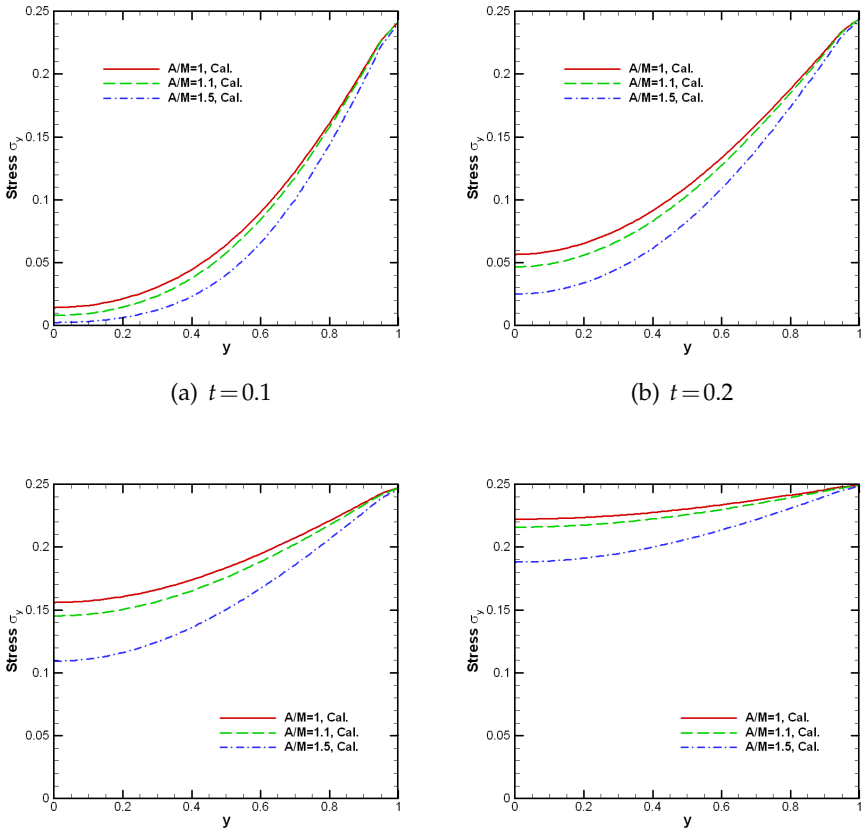
Fig. 5 shows the computed vertical stress distributions with different time in y-direction for the three states of $r_c=1$, 1.1 and 1.5 corresponding to Fig. 3, illustrating that both the changes and the lag effects of the stress and temperature are synchronized.

Combined with Figs. 3-5, we can see that in the mutual coupling state of temperature and displacement field, the temperature, displacement, resultant strain and stress distributions interact with each other, and the lag phenomena is clearly observed, which is consistent with the descriptions of Yang and Chen [29].

4.2 Solving 2D transient heat flow problem for an infinite cylinder

In order to further validate the present finite-element algorithm, the two-dimension transient heat flow for the infinite cylinder has been simulated, in which the same states are from [26]. Consider the infinite cylinder with unit radius (Fig. 6(a)), which is initially at a uniform absolute temperature T_0 throughout. For $t>0$, the temperature of the outer surface ($y=1$) is maintained at $T=T_0+\theta_0$, i.e. the increment is θ_0. There are no vibration,

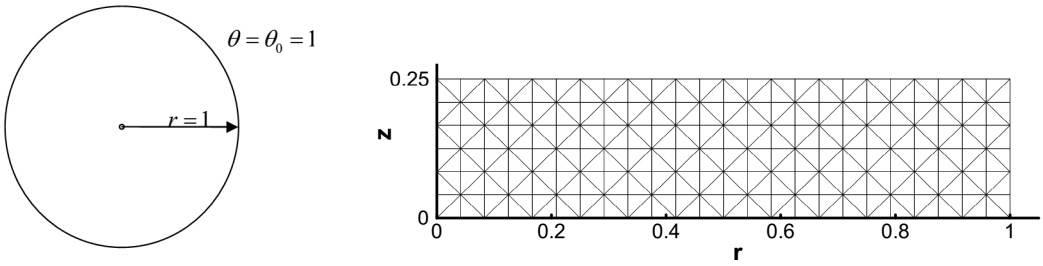
https://doi.org/10.4208/cicp.270515.010216a Published online by Cambridge University Press



(a) $t=0.1$ (b) $t=0.2$

(c) $t=0.5$ (d) $t=1.0$

Figure 5: Time history of the vertical stress σ_y in y-direction with different coupling ratio r_c.

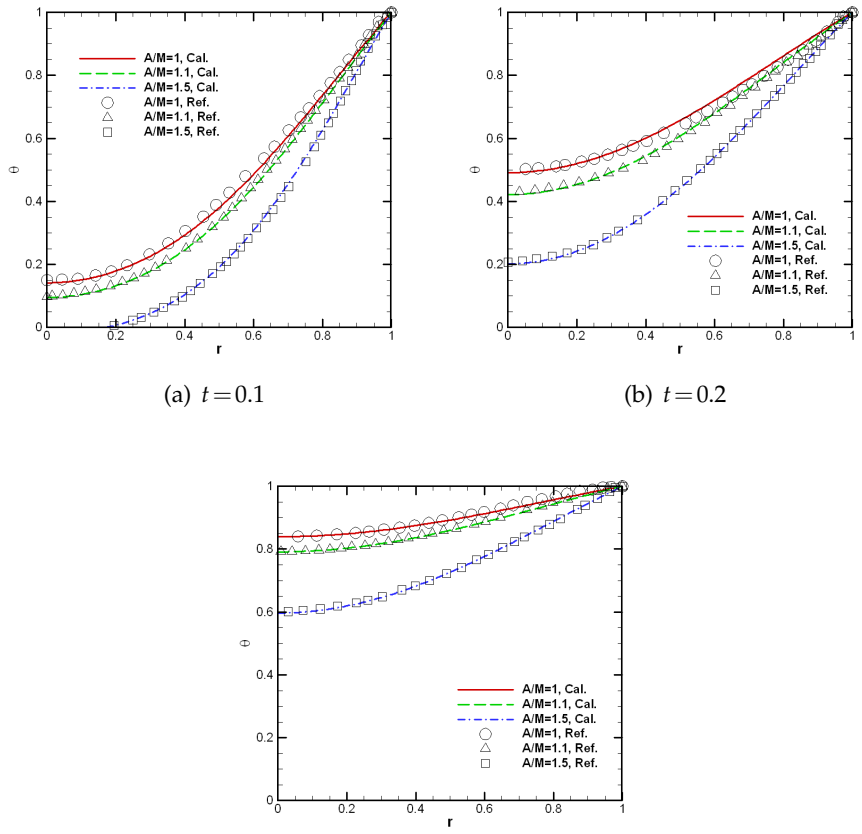


(a) Infinite cylinder with initial temperature $\theta=\theta_0=1$ at $r=1$

(b) Triangular mesh of rectangle domain

Figure 6: Computational model of axisymmetric dynamic thermoelasticity problem and the corresponding mesh, with nodes number 126 and elements number 200 on domain $A=[0,1]\times[0,0.25]$.

https://doi.org/10.4208/cicp.270515.010216a Published online by Cambridge University Press



(a) $t=0.1$ (b) $t=0.2$

(c) $t=0.4$

Figure 7: Time history of the temperature distributions along with r-direction in different coupling ratios r_c.

body force, heat source, external traction force or boundary flux. We will simulate its transient temperature distribution and deforming performance.

The computation domain in [26] is a quarter of a circle. Here we use the axisymmetric plane of a cylinder chosen as the rectangle domain $[0,1]\times[0,0.25]$. The finite-element mesh is shown in Fig. 6(b) and the non-dimensional coefficients are the same as (4.3).

For the boundary conditions, along $r=1$, the initial temperature increment $\theta=\theta_0=1$, and the rest boundaries are insulated. As the cylinder is infinite in z-direction, then we fix the normal displacement on up-down boundaries of $z=0.25$, all the displacement components on $r=0$ are set as the axisymmetric condition, and the circle boundary $r=1$ is free.

The temperature increment in the radial direction at the time $t=0.1$, 0.2 and 0.4 with different coupling ratio $r_C=1$, 1.1 and 1.3 are illustrated in Figs. 7(a)-(c). The curves are the computed results in this paper and the symbols denote the data from [26]. The good

https://doi.org/10.4208/cicp.270515.010216a Published online by Cambridge University Press

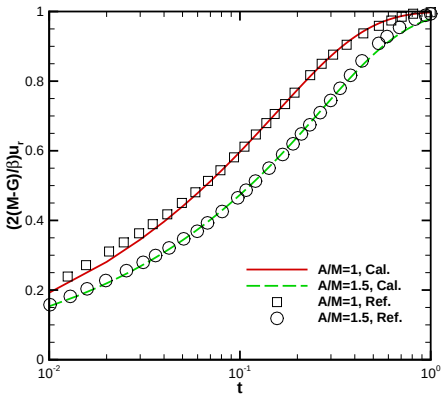


Figure 8: Time history of the surface expansion of the infinite cylinder at $r_c=1$ and 1.5.

agreement also demonstrates the accuracy and reliability of the current finite-element algorithm. It is seen that as a result of the increment of the temperature, the heat expansion of the body occurs, and the volumetric change behaves as a lag to slow down the temperature increment. The higher becomes the coupling degree, the more obvious is the lag effect. As the time increases from $t=0.1$ to 0.4, the process of heat conduction approaches to the steady state, and in the last, the temperature of the domain throughout reaches the given value $T=T_0+\theta_0$.

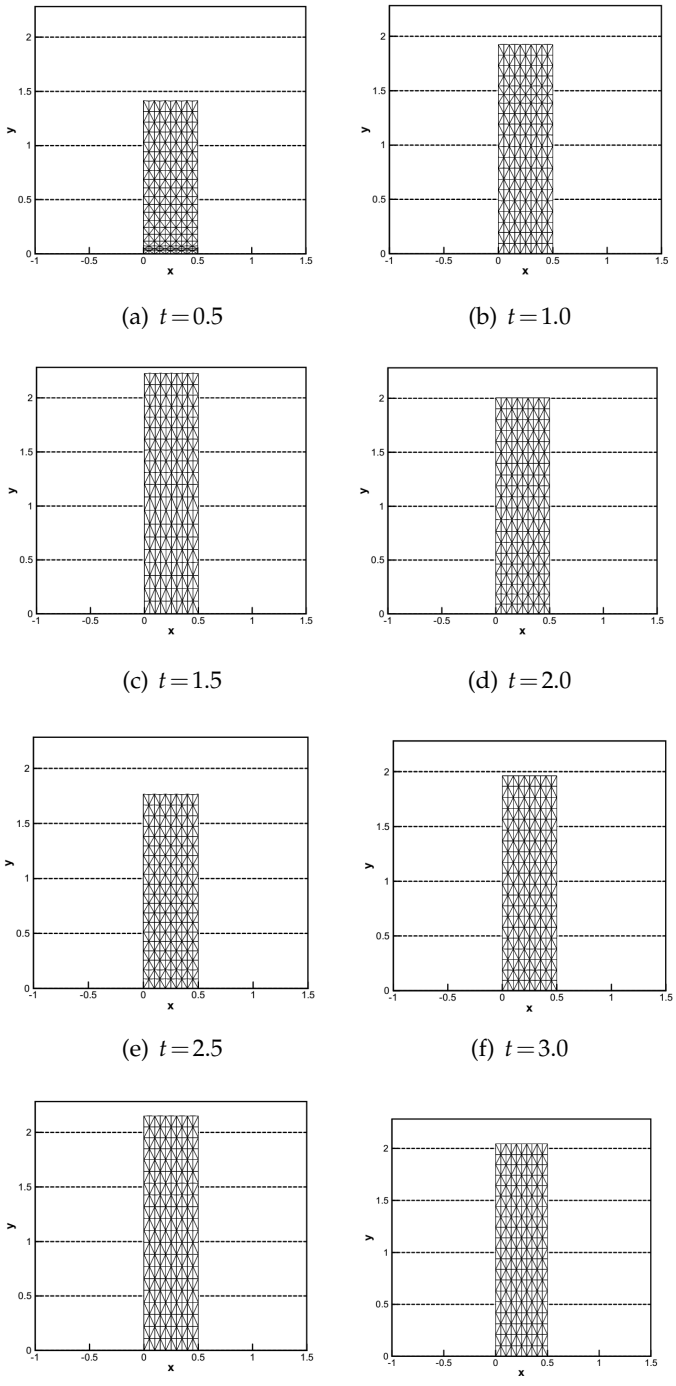
Fig. 8 shows the comparison of the time history of the normalized vertical displacement between the present computation (lines) and the results (symbols) from [26] at $r_c=1$ and 1.5. The good agreement of the two results also validates the correctness and precision of the present finite-element algorithm in computing the thermal-induced deformation in the cylindrical coordinate.

4.3 Solving 1D transient heat flow with vibration and damping effect

In this subsection, we perform the computation with elastic vibration using the scheme Eq. (3.27). The computational model, material coefficients, the initial and boundary conditions are chosen the same as the computation in Subsection 4.1, besides that the inertia term is added up to the displacement field. Now from Fig. 1, the DC-Vib-Incl and SC-Vib-Incl methods are used, respectively.

At first, we neglect the damping term and focus on the vibration effect of the coupling term on both dynamic and heat equations. The deforming process of the material layer at different time is illustrated in Fig. 9 for the coupling state $r_c=1.5$. Since the transient effect is considered, initially there is a sudden increase of the temperature on the outer surface and the layer is subjected to a volume load, producing an instantaneous acceleration. In Figs. 9(a) and (b), an longitudinal elasticity wave propagates in the negative y-direction, and the wave front arrives at the bottom and reflects with elastic rebound in the time $t=$

https://doi.org/10.4208/cicp.270515.010216a Published online by Cambridge University Press



(a) $t=0.5$ (b) $t=1.0$

(c) $t=1.5$ (d) $t=2.0$

(e) $t=2.5$ (f) $t=3.0$

(g) $t=3.5$ (h) $t=4.0$

Figure 9: Time history of deformations of the domain at $r_c=1.5$, the amplified scale is M/β.

https://doi.org/10.4208/cicp.270515.010216a Published online by Cambridge University Press

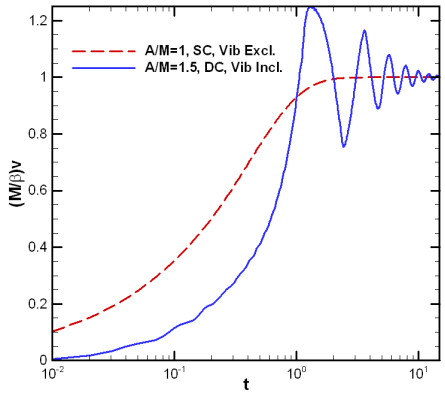


Figure 10: Time history of outer surface expansion at $r_c = 1.5$ using the DC-Vib-Incl with comparison of the SC-Vib-Excl method.

0.5 to 1.0. In the contrast with the steady state arrived after about time $t = 1$ in Subsection 4.1, the vibration of the outer surface still exists, shown in Fig. 10. As the time goes on, the amplitude of the wave becomes smaller, and the whole system reaches the same energy balance as the steady state in Subsection 4.1.

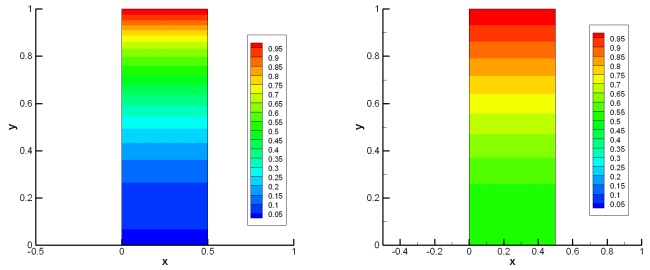
The time history of increment of temperature is shown in Fig. 11. Caused by the displacement oscillation, the vibration of the temperature also exists. The most significant feature is the climb after a decline of the value from time $t = 0.5$ to 1.0 shown in Fig. 12 at the bottom ($y = 0$), corresponding to the reflection of the elastic wave in Figs. 9(a) and (b). For $t > 1.0$, the temperature field gradually approaches to the steady state, with oscillating behavior.

For different ratios, the vibrations of both displacement field and temperature increment are shown in Fig. 13. It can be observed that, the smaller is the value of r_c, the less becomes the portion of energy transformation from elastic energy to heat energy, and the longer goes on the vibration. However, the system will still reach the steady state finally. Especially, considering the decoupled case $r_c = 1$, the result of the temperature solved by DC-Vib-Excl is the same as the one obtained using the SC-Vib-Excl method, while the thermal-induced vibration of the displacement continuously exists (red line in Fig. 13(b)).

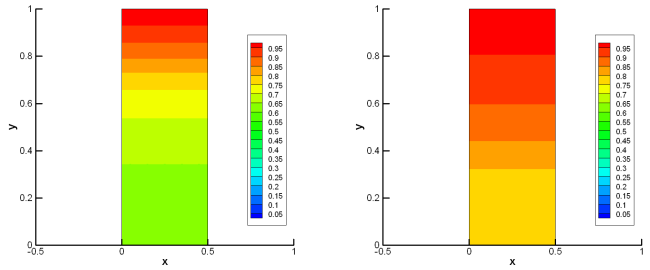
With different line types, Fig. 14 shows the vibration results obtained by all four finite-element methods. In Fig. 14(a), the displacement field will finally reach the steady state, except for the results from the SC-Vib-Incl method, and once the transformation from elastic energy to heat energy occurs, the steady state will be reached finally. For the temperature increment in Fig. 14(b), we can see that the steady results can always be reached, because the conducting diffusion process is irreversible essentially.

Fig. 15 shows the stress distributions in y-direction at various time $t = 0.1 \sim 0.4$ obtained by four coupled thermoelasticity methods. In the methods considering vibration, the propagation and reflection of elastic wave can be also predicted. In the SC-Vib-Incl

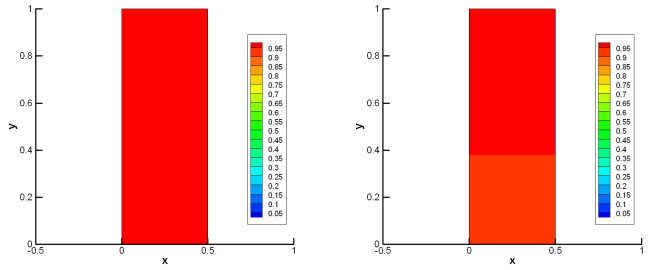
https://doi.org/10.4208/cicp.270515.010216a Published online by Cambridge University Press



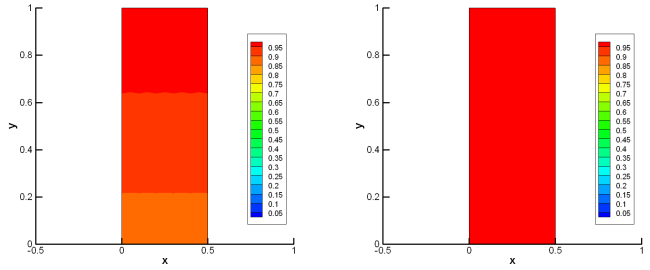
(a) $t=0.5$ (b) $t=1.0$



(c) $t=1.5$ (d) $t=2.0$



(e) $t=2.5$ (f) $t=3.0$



(g) $t=3.5$ (h) $t=4.0$

Figure 11: Time history of the temperature increment distribution at $r_c=1.5$.

https://doi.org/10.4208/cicp.270515.010216a Published online by Cambridge University Press

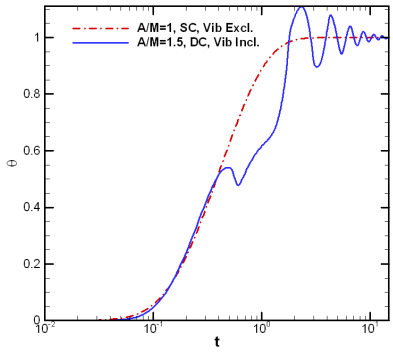
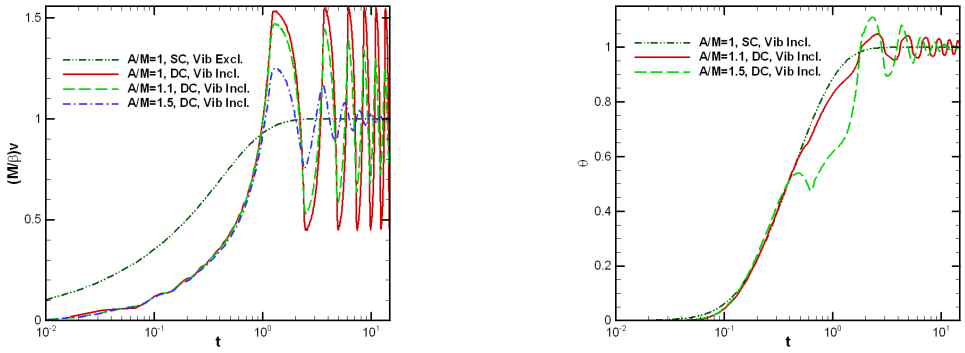
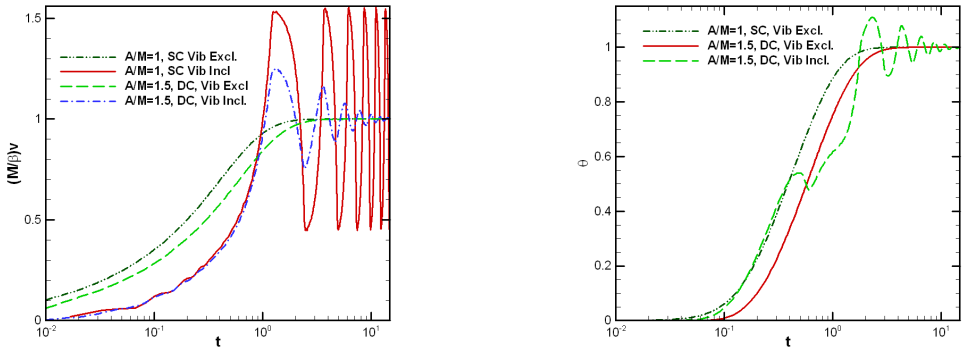


Figure 12: Time history of temperature increment at the bottom ($y=0$) and comparison with results of the SC-Vib-Excl method.



(a) Time history of the outer surface vibration (b) Time history of the temperature increment at $y=0$

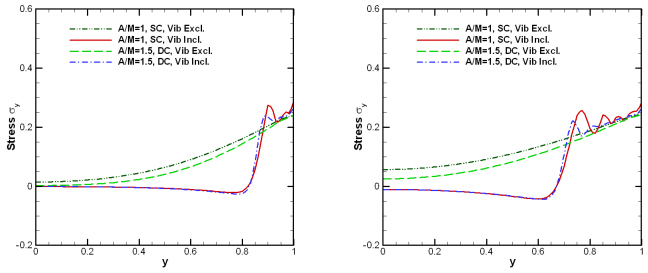
Figure 13: Comparison of the results from the DC-Vib-Incl method at different r_c.



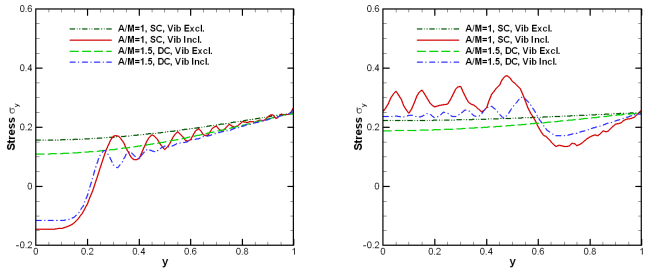
(a) Time history of the outer surface vibration (b) Time history of the temperature increment at $y=0$

Figure 14: Comparison of the results from the four coupled thermoelasticity methods.

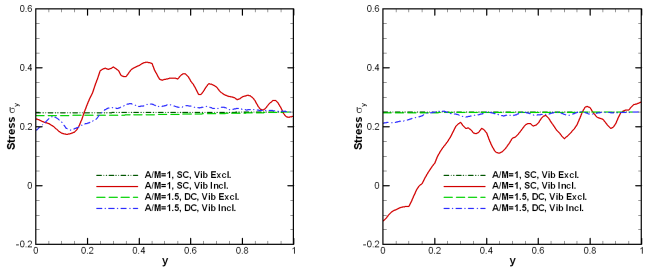
https://doi.org/10.4208/cicp.270515.010216a Published online by Cambridge University Press



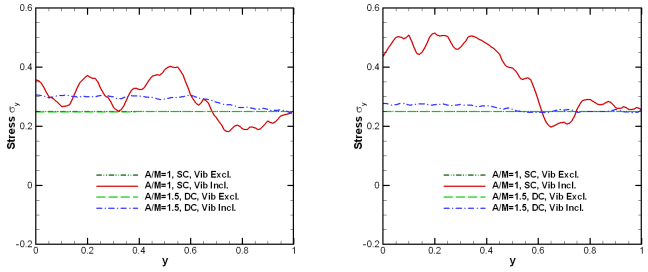
(a) $t=0.1$ (b) $t=0.2$



(c) $t=0.5$ (d) $t=1.0$



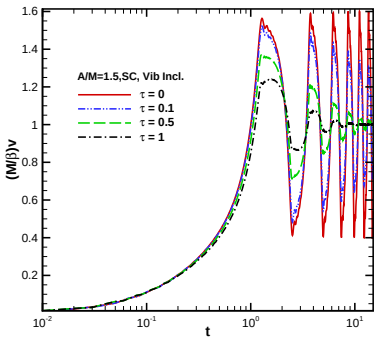
(e) $t=2.0$ (f) $t=3.0$



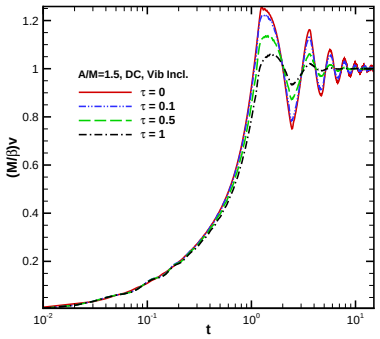
(g) $t=3.5$ (h) $t=4.0$

Figure 15: Comparison of stress σ_y distribution with $t=0.1\sim4$ obtained by the four coupled thermoelasticity methods.

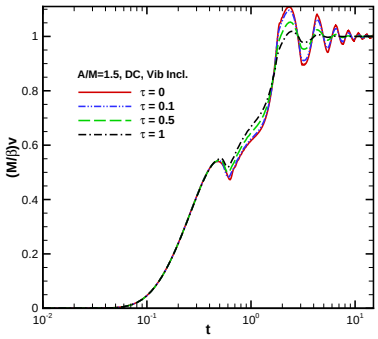
https://doi.org/10.4208/cicp.270515.010216a Published online by Cambridge University Press



(a) Time history of the outer surface vibration by the SC-Vib-Incl method.



(b) Time history of the outer surface vibration by the DC-Vib-Incl method



(c) Time history of temperature increment at $y=0$ by the DC-Vib-Incl method

Figure 16: Comparison of oscillating behavior of vertical displacement and temperature increment with different damping effects.

method, the temperature-induced elastic energy can't be dissipated, so the vibration exists all the time, while the stress field will approach to the same steady results obtained by other methods.

From the results above, it is noted that even without the damping matrix $\mathbf{C_u}$ in the dynamic thermoelasticity equation, once the coupling matrix $\mathbf{L}$ is presented, the whole system will finally reach the steady state. Now we add the damping matrix accounting for dissipation of energy to the computational schemes to make the models more realistic. For simplicity, we only use the form of $\mathbf{C_u}$ as Eq. (3.14). Fig. 16 shows the vibration of the outer surface and temperature increment with the non-dimensional damping coefficients of τ=0, 0.1, 0.5 and 1 in different line types. In the uncoupled state illustrated in Fig. 16(a), the thermal-induced vibration will never dissipate as the red solid line with $\tau=0$ until the damping term is added, i.e., $\tau>0$, while in the coupled state, from Fig. 16(b) to

https://doi.org/10.4208/cicp.270515.010216a Published online by Cambridge University Press

Fig. 16(c), the energy dissipation comes from both the damping effect in the dynamic thermoelasticity equation and the coupling term in the heat conductive equation, which makes the convergence speed much faster. On the other side, it is seen that, although the damping effect is introduced with an extra computational cost, both the damping effect and the coupling term in the heat conduction equation can improve the stability of the algorithm, and the main reason for this improvement needs to be further investigated, depending on both r_c and τ.

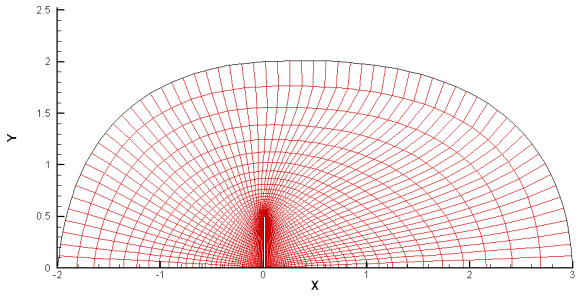
From the numerical examples in Subsections 4.1-4.3, it is shown that the four finite-element methods presented in Fig. 1 have been demonstrated to be reliable and accurate in computing the temperature distribution, elastic deformation and stress changes for the thermoelastic material, which becomes as the foundation to develop the efficient computable model and algorithm to simulate the dynamic response and deformation of the uncontrolled spacecraft and further help predicting its failure and damage in strong aerodynamic heating and force environment.

4.4 Coupled thermoelasticity analysis of a plate in hypersonic re-entry flow

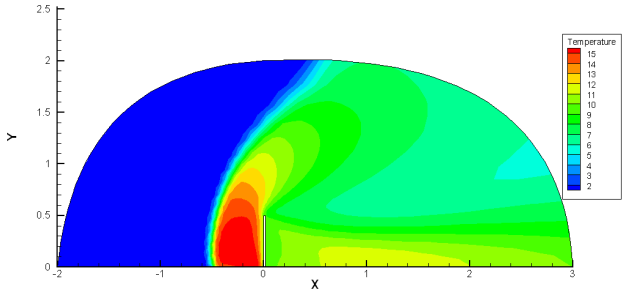
In this subsection, we apply the present finite-element methods to the simulation of the heat conduction and deformation of the structure subjected to hypersonic aerothermodynamic environment. For simplicity, the aerothermodynamic results are assumed to have been obtained by the numerical methods of aerodynamics covering various flow regimes [38–42, 52–54]. So we directly take the values of the computed aerothermodynamic temperature and force as the boundary conditions for the coupled thermoelasticity problem and obtain temperature and stress distributions of the inner structure of hypersonic flying body.

To combine the present methods with the gas-kinetic unified algorithm (GKUA) [38–42] for solving the Boltzmann model equation, we consider the flow-rounded infinite plate problem as an example of thermodynamic coupling response during spacecraft re-entering Earth's atmosphere, shown in Fig. 17. The size of the plate is $0.015m \times 0.5m$, the exterior of which is the reentry near-continuous transition flow, the inflowing Mach number, Knudsen number and ratio of specific heat are $Ma_\infty = 8.37$, $Kn_\infty = 0.01$ and $\gamma = 1.4$, respectively. The exterior flow field of the plate with the mesh of 63×41 in the XoY coordinate system is computed [41] by the GKUA for solving the Boltzmann model equation with rotational non-equilibrium effect. Because of the re-entry near-continuum transition flow regime, the thick detached shock wave layer is formed around the thin plate shown in Figs. 17(b) and (c), and strong aerodynamic heating and force are imposed as the interface condition of the present thermodynamic coupling finite-element algorithm on the plate surface. The high temperature and strong pressure make the plate expand and deform. Without considering the vibration, the outer boundary value of the coupled thermoelasticity problem are provided by the surface temperature and pressure from the GKUA, the inner boundary ($y = 0$) shown in Fig. 18(a) is fixed and insulated. We now try to solve this kind of dynamic thermoelasticity coupled problem.

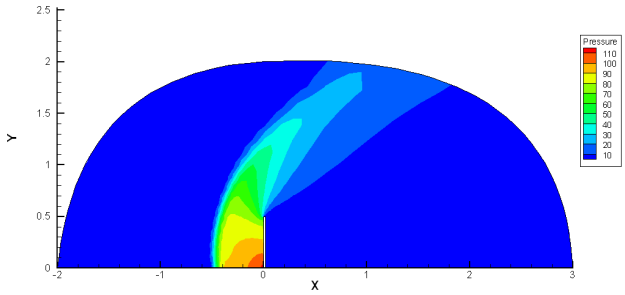
https://doi.org/10.4208/cicp.270515.010216a Published online by Cambridge University Press



(a) Computed mesh of the flow field around the vertical plate



(b) Temperature distribution of the exterior flow field of the plate

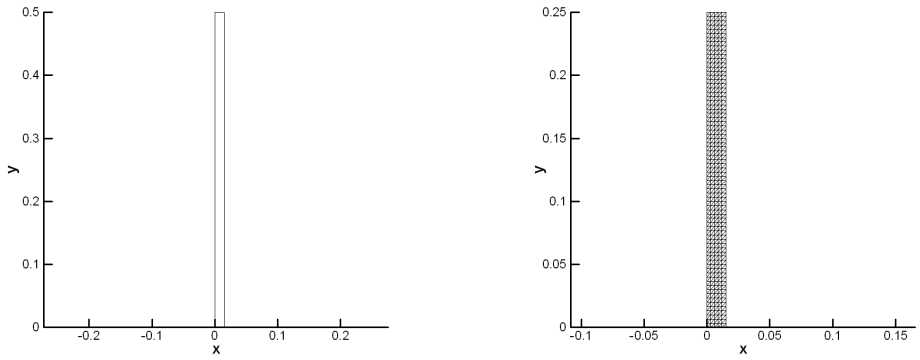


(c) Pressure distribution of the exterior flow field of the plate

Figure 17: Reentry hypersonic flow field of the vertical plate in near-continuum transition flow regime solved by the GKUA with $Kn_\infty = 0.01$, $Ma_\infty = 8.37$.

The mesh generation is carried out and the computational mesh is shown in Fig. 18(b) for the inner structure of the vertical plate section. Usually, the nodes of the solid mesh on the plate surface should be consistent with the boundary nodes of the flowfield mesh [6], which comes from the conforming mesh methods [17]. To make the thermoelastic computation more precise and dependable, the finer mesh is generated for the plate. Because

https://doi.org/10.4208/cicp.270515.010216a Published online by Cambridge University Press



(a) Coupled thermoelasticity domain of plate (b) Portion of plate finite-element mesh

Figure 18: Plate domain and computational mesh with the node number 906 and element number 1500 on domain $[0,0.015]\times[0,0.5]$.

of the incompatibility of the two different meshes on the interface between the computational mesh of the exterior flow field around the plate and the present dynamic thermoelasticity computational mesh in the inner structure of the plate, linear interpolation is used from the flow field mesh to the plate mesh to approximate the value of temperature and pressure on the plate surface, that is, for each node on the surface of the plate mesh, we try to find out the line segment on the boundary of the flowfield mesh where the node lies, treat this line segment as the one-dimensional element, apply the linear shape function to this element, and finally combine with the temperature and pressure data on the two ending nodes, then obtain the values of the temperature and pressure.

For this case, as the steady results are given by the GKUA and the final temperature and pressure distribution are obtained in Fig. 17, here we directly apply the temperature and the force boundary condition on the plate, instead of the heat flux condition, since the prescribed temperature condition can also simulate the strong heating process and produce the vibration of both the displacement and temperature as Prevost [27] and in Subsection 4.2. Assume initially the plate is at the temperature T_0, and the outer flow field has been in steady state. For $t>0$, the temperature of the plate outer surface then reaches $T=T_0+\theta$, where T is the computed temperature obtained by the GKUA, from which the temperature increment is $\theta=T-T_0$.

The non-dimensional model is usually adopted for the computation of the exterior flow field of hypersonic aerothermodynamics because of the multi-scale effect covering various flow regimes with different flying heights during the re-entry process. It is needed to convert the non-dimensional aerothermodynamic data from the GKUA into the actual temperature and pressure for the dynamic thermoelasticity coupling computation on the surface of the flying body. Here, the Boltzmann model equation provides the statistical description of the gas flow in any non-equilibrium state from the level of the kinetic theory of gases by catching the time evolution and update of the molecu-

https://doi.org/10.4208/cicp.270515.010216a Published online by Cambridge University Press

lar velocity distribution function f in the position space $\overrightarrow{r}=(x,y,z)$ and velocity space $\overrightarrow{V}=(V_x,V_y,V_z)$. The unified Boltzmann model velocity distribution function equation can be non-dimensionalized and numerically solved by using the discrete velocity ordinate technique and the gas-kinetic finite-difference numerical scheme [38–42]. Once the discrete velocity distribution functions $f_{\sigma,\delta,\theta}$ are solved at each of discrete velocity ordinate points $(V_{x\sigma},V_{y\delta},V_{z\theta})$, all of the macroscopic flow variables of aerothermodynamics including the temperature and pressure denoted by T^* and p^* at any time in each point (x_i,y_j,z_k) of the flow field can be evaluated and updated by the appropriate discrete velocity quadrature method on the basis of the moments of the velocity distribution function over the molecular velocity space. Finally, the actual temperature T and pressure p should be obtained by

$$T=T^*T_\infty,\quad p=p^*\left(\frac{1}{2}\rho_\infty V_\infty^2\right),$$

where T_∞, ρ_∞, and V_∞ are the reference temperature, gas density and velocity of the inflowing flow, respectively.

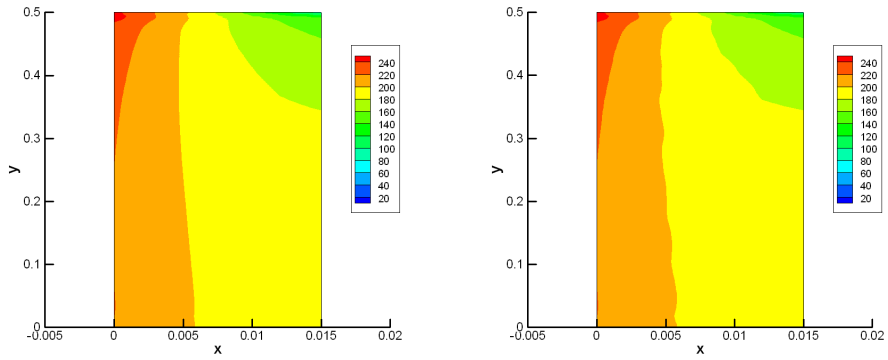
The plate is chosen as steel, the following are the property parameters of material,

$$E=2.06\times10^{11}Pa,\quad \nu=0.3,\quad \alpha=1.5\times10^{-6}/^\circ C,$$
$$\rho=7850kg/m^3,\quad c=460J/(kg\cdot^\circ C),\quad k=50W/(m\cdot^\circ C).$$

The reference temperature is set as $T_0=500^\circ C$, and the time step is taken as $\delta t=0.05s$ with the computational time of $\overline{T}=5s$. Figs. 19(a) and (b) show the temperature distribution in the inner structural field of the plate at time t=5s computed by the present SC and DC methods, respectively. It is noted that the temperature field has not reached the steady state in the DC case while it has become to be stable for the SC method to compute the temperature distribution.

The temperature correlation between the exterior flow field and the inner structure of the plate is shown in Fig. 20 with different Y-direction locations of $y=0.05$, 0.25 and 0.45, where the temperature distribution from the windward and leeside regions in the exterior flow field of the plate is solved [41] by the GKUA based on the Boltzmann model equation. It is indicated that the above-mentioned temperature on the windward and leeside surface is in good agreement with the surface temperature from the inner structural field of the plate computed by the present dynamic thermoelasticity coupling finite-element algorithm, which verifies the correctness and accuracy of the present computable models and procedure realization for the dynamic thermoelasticity coupling problems. The temperature in the stagnation point (origin point) is higher than the nearby region, while the most highest point is on the left top of the plate, as it has the maximum curvature variation and is subjected to the most severe aerothermodynamic heating, then the heat flux of the flow field becomes as the maximum value on the left top of the plate, and the temperature in the inner of the material also rises to the maximum. Consequently, the temperature emerges the obvious change on the windward boundary surface of the

https://doi.org/10.4208/cicp.270515.010216a Published online by Cambridge University Press



(a) Results by the SC-Vib-Excl (b) Results by the DC-Vib-Excl

Figure 19: Comparison of temperature increments in the inner of the plate with the SC and DC methods at time $T=5s$.

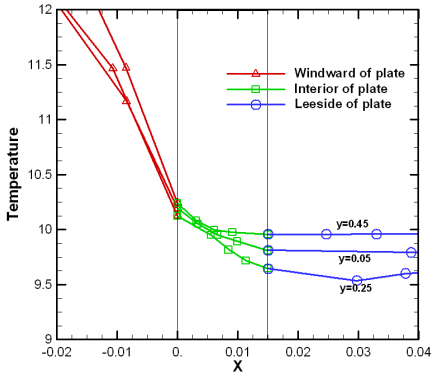
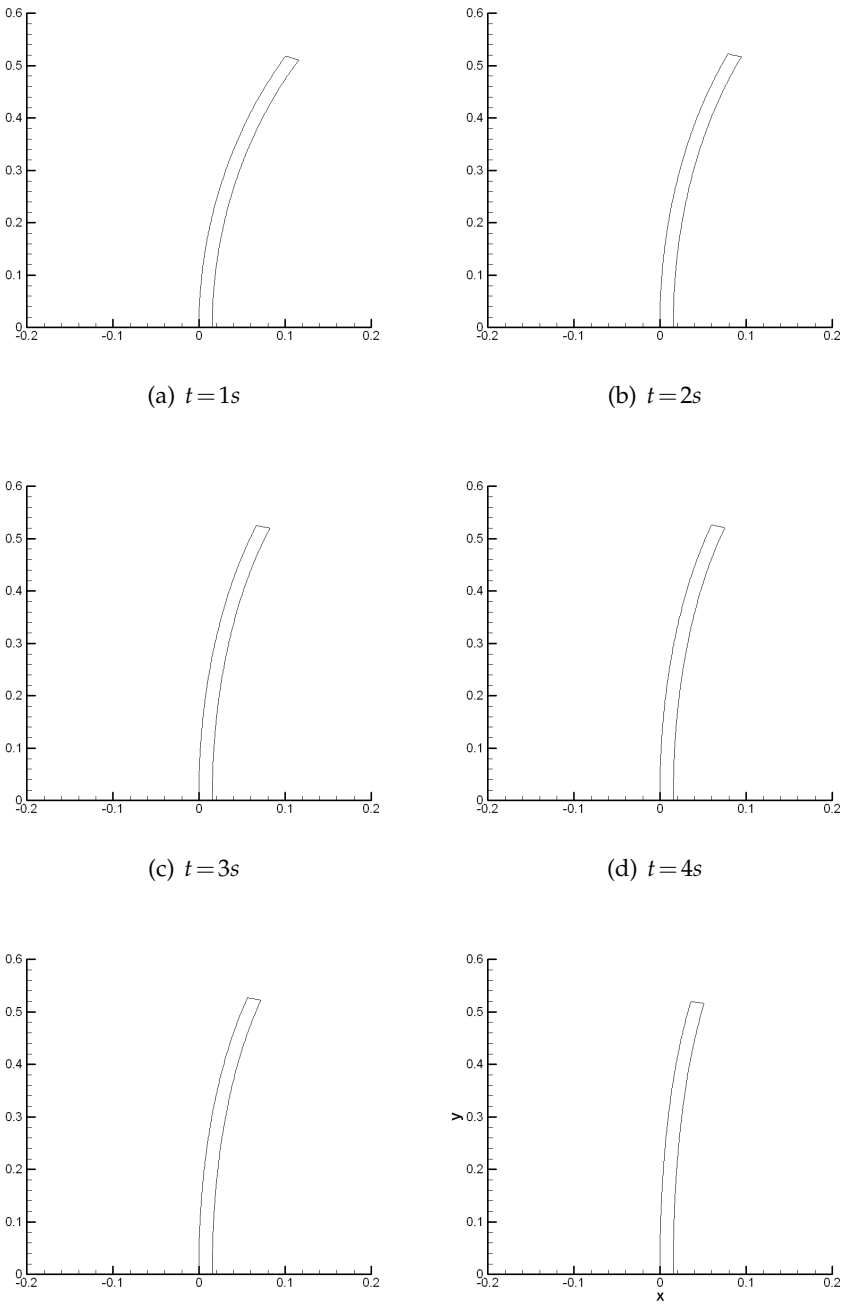


Figure 20: Temperature correlation along with X at different Y-direction locations of $y=0.05$, 0.25 and 0.45 between the exterior flow field and the inner structure of the plate.

plate, and this change is also clearly appeared in the inner field of the material structure. Fig. 20 authenticates this changing characteristics with three curves corresponding to $y=0.05$, 0.25 and 0.45.

By the hypersonic reentry flow around, the plate is subjected to both the strong aerodynamic heating and force. Fig. 21 shows the time history $t=1s\sim5s$ and the final stable state of the plate deformation computed by the present DC method. It is observed that, under the dual interaction of high temperature and large pressure difference between the windward and leeside of the plate with the exterior flow field of hypersonic strong aerothermodynamic environment, the plate firstly bends to the leeside to a large extent, in which the windward pressure higher than the leeside one is imposed instantly to the plate. Then the aerothermodynamic heating makes the continual increase of tempera-

https://doi.org/10.4208/cicp.270515.010216a Published online by Cambridge University Press



(a) $t=1s$ (b) $t=2s$

(c) $t=3s$ (d) $t=4s$

(e) $t=5s$ (f) Steady state

Figure 21: Time history of the plate deformation computed by the DC method (a)-(e) and the steady state (f), the displacement is amplified by 50 times.

https://doi.org/10.4208/cicp.270515.010216a Published online by Cambridge University Press

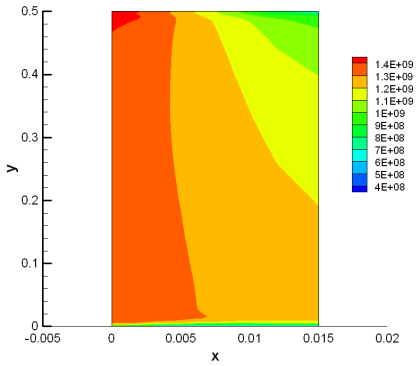
ture, and produces the sustained thermal expansion in the inner structure of the plate, which leads to inhomogeneous thermal stress distributions. The higher temperature in the windward side of the plate produces more thermal expansion and heat stress along with the opposite direction of the pressure than the leeside one. As the time goes on, the net force of the outer pressure and the inner heat stress makes bending amplitude of the plate a little bit smaller than the initial one. As it is stated previously that at $t=5s$, the temperature does not reach the steady state computed by the DC method yet, the thermal expansion continues afterward and finally arrives at the stable state shown in Fig. 21(f), which is the same as the final steady state computed by the SC method. By the chosen material property coefficients, the coupling ratio is $r_c = M/A \approx 1.034$ for the defined dynamic thermoelasticity problem and it is seen that there is hardly any difference between these two results. Although it is more accurate to reflect the real coupled thermoelasticity state of the structure by the DC method, using the SC method is also reasonable if only attention to the final stable state of the structure is paid, and in the engineering practice, the SC method is widely used with less computational cost and more efficiency.

Fig. 22 shows the stress distribution of the plate in the steady state of $Kn_\infty = 0.01$, $Ma_\infty = 8.37$ under the re-entry hypersonic aerothermodynamic environment corresponding to the computed state shown in Fig. 21(f), it can be seen that both the normal stress σ_x and σ_y are dependent on the temperature distribution. The maximum shear stress and Von Mises stress shown in Figs. 22(c), (d) and (e) appear in the leeside of the plate in the bottom. From the external plate-surface temperature and pressure distribution of flow fields computed by the GKUA (shown in Figs. 17(b) and (c)), the increase of surface temperature and pressure (compared to the inflow values) of the windward area for the left side flat plate is larger than those of the leeward area for the right side flat plate. From the analysis of the deformation in Fig. 21, we conclude that the thermal expansion in the windward side of the plate is suppressed by the pressure while it is subjected to the maximum temperature variation on the left top of the windward side and the minimum outer pressure in the leeside of the plate. The flat plate deforms and bends toward the leeward direction of the flat plate because of the dual role of the dynamic thermoelasticity coupling, which may cause the nonlinear deformation and failure of flying body during hypersonic uncontrolled reentry.

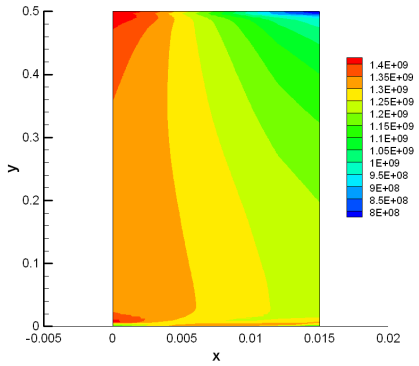
5 Concluding remarks

Based on the dynamic thermoelasticity and the heat conductive equations, the weak form of dynamic thermoelasticity coupling model is derived by the variational principle. The Newmark implicit method is constructed to numerically discretize the velocity and acceleration terms of the dynamic equation, and the second-order Crank-Nicolson scheme is devised to deal with the weak form of the heat conductive equation, then the finite-element implicit schemes are constructed for various dynamic thermoelasticity coupling cases, as a result, the corresponding finite-element algorithm and computational proce-

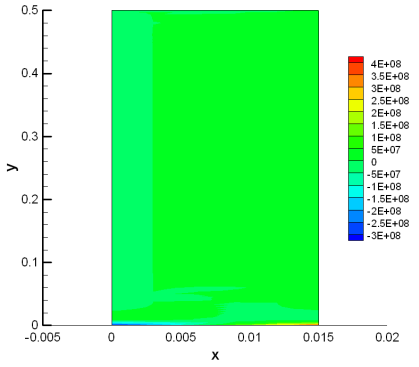
https://doi.org/10.4208/cicp.270515.010216a Published online by Cambridge University Press



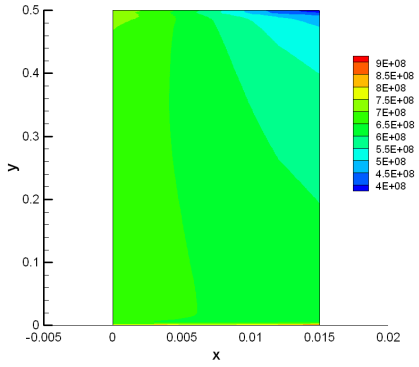
(a) Normal stress component σ_x



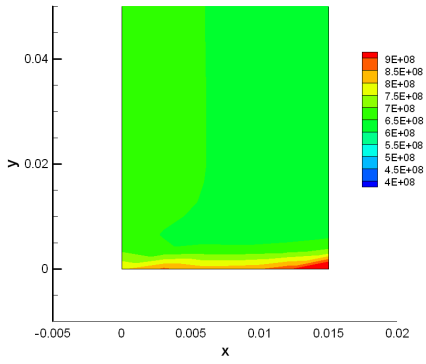
(b) Normal stress component σ_y



(c) Shear stress component τ_{xy}



(d) Von Mises stress σ_s



(e) Von Mises Stress at bottom

Figure 22: Stress distribution of the plate in the steady state of $Kn_\infty = 0.01$, $Ma_\infty = 8.37$.

https://doi.org/10.4208/cicp.270515.010216a Published online by Cambridge University Press

dures have been established to simulate the transient thermal and mechanical behaviors of the structures with strong aerodynamic heating and force environment. As the numerical tests, the one-dimension transient heat flow with vibration and damping effect and two-dimensional transient heat flow of the infinite cylinder authenticate the correctness and reliability of the present algorithm in computing the transient thermodynamic coupling problems, the difference and connection between the DC and SC methods are discussed, and the local oscillating of the elastic wave can be accurately captured. It is also important to note that even if the damping term is not considered in the dynamic thermoelasticity equation, the energy transformation from elasticity to heat, which is the coupling term presented in the heat conductive equations, acts also as a damping effect and causes the attenuation of elastic wave.

Incorporated with the gas-kinetic unified algorithm based on the Boltzmann model equation for solving the exterior hypersonic flow field, the finite-element computation for the dynamic coupling thermoelasticity response of the re-entry flow around plate has been carried out. It is indicated that during the computational process of thermodynamic coupling response, the increase of surface temperature and pressure (compared to the inflow values) of the windward area for the left side flat plate is larger than those of the leeward area for the right side flat plate. The flat plate deforms and bends toward the leeward direction of the flat plate because of the dual role played by the thermodynamic coupling, which demonstrates the unsteady changing process and influencing mechanism of the induced object-bending deformation once the uncontrolled and flying body is within the strong aerodynamic thermal flow environment.

Actually, the dynamic thermoelasticity coupling of the structure is the two-way energy transformation process. The heat is transferred by conduction, converted into the elastic energy and causes the oscillation if inertia force is considered. Conversely, part of the elastic energy is converted into heat and further transferred by conduction. With this continuously transferring process, the final steady state is reached with the energy balance between the internal and external of the system. It is seen in the numerical computation that the SC-Vib-Excl method uses the shortest time to ”arrive at” the end point. The final result is right, but details of the bidirectional transformation process of the energy are totally neglected. The DC-Vib-Excl method gives a better correction of the SC-Vib-Excl method. The reason why the vibration is not taken into account is that the heating or loading is imposed slowly and the elastic energy transformation to heat has finished within a single time step. So if we consider the fast heating or loading on the structure, vibration happens and the DC-Vib-Incl method is the most accurate. Nevertheless, it is difficult to simulate and analyze the vibrating behavior when the computation involves the complex geometry, like the reentry spacecraft with complicated configuration, and the methods that do not contain the vibration are reasonable to capture the global thermal and mechanical behaviors. As a result, the SC-Vib-Excl and DC-Vib-Excl methods are usually used in the engineering and the former is preferred for its less computational cost.

As the first attempt, the computational analysis tool for the dynamic thermoelasticity

https://doi.org/10.4208/cicp.270515.010216a Published online by Cambridge University Press

coupled system of heat transfer, deformation and stresses on uncontrolling and flying body under reentry aerothermodynamic environment has been developed in this work. In fact, the coupling between the fluid and the structure is a complicated process. For simplicity, the dynamic simulation considered in this paper only involves the structural computation with the boundary conditions provided by the exterior flow field and the fixed surface temperature and pressure on the boundary. In the practical application, the unsteady flow should be considered, and in that situation, the surface temperature and pressure in dynamic state and real time will be more compatible with the real physics. The actual heat flux boundary condition with convection and radiation should include the outer temperature computed from the fluid field and should be treated as T_{ext} in Eq. (2.15), and the aerodynamic force and heating should be performed by transferring the hypersonic flow pressure and temperature conditions to the boundary of the solid body. The actual temperature increment and stress distribution by this consideration may well reflect the real physical phenomena, which becomes our future work.

Acknowledgments

This work is supported by the National Key Basic Research and Development Program (2014CB744100) and the National Natural Science Foundation of China (11325212, 91530319 & 91016027), and also supported by China Postdoctoral Science Foundation (2014M562616). The first author would like to thank Prof. Weinan E for helpful discussion about metal melting, materials' phase transition and nonlinear behavior of structural response. The authors are particularly thankful to the reviewers and editor for their valuable comments and suggestions, which greatly improved the quality of the manuscript.

References

[1] R.P. Hoyt, R.L. Forward, Performance of the Terminator Tether for autonomous deorbit of LEO spacecraft, AIAA 99-2839, 35th AIAA/ASME/SAE/ASEE Joint Propulsion Conference & Exhibit, June 20∼24, 1999.
[2] C.M. Reynerson, Reentry Debris Envelope Model for a Disintegrating, Deorbiting Spacecraft Without Heat Shields, AIAA 2005-5916, AIAA Atmospheric Flight Mechanics Conference and Exhibit, Aug. 15∼18, 2005, 10.2514/6.2005-5916.
[3] Y. Prevereaud, J.L. Vérant, J.M. Moschetta, F. Sourgen, M. Blanchard, ebris Aerodynamic Interactions during Uncontrolled Atmospheric Reentry, AIAA Atmospheric Flight Mechanics Conference, 2012, 10.2514/6.2012-4582.
[4] M. Reyhanoglu, J. Alvarado, Estimation of debris dispersion due to a space vehicle breakup during reentry, Acta Astronautica 86 (2013) 211-218.
[5] D. Balakrishnan, J. Kurian, Material thermal degradation under reentry aerodynamic heating, J. Spacecraft & Rockets 51 (2014) 1-10.
[6] B.J. Thuruthimattam, P. P. Friedmann, J. J. McNamara, K. G. Powell, Modeling approaches to hypersonic aerothermoelasticity with application to reusable launch vehicles, 44th

https://doi.org/10.4208/cicp.270515.010216a Published online by Cambridge University Press

AIAA/ASME/ASCE/AHS/ASC Structures, Structural Dynamics, and Materials Conference, 7-10 April 2003, Norfolk, Virginia.
[7] P. P. Friedmann, J. J. McNamara, B. J. Thuruthimattam, K. G. Powell, Hypersonic aerothermoelasticity with application to reusable launch vehicles, 12th AIAA International Space Planes and Hypersonic Systems and Thechnologies, 15-19 December 2003, Norfolk, Virginia.
[8] J. J. McNamara, B. J. Thuruthimattam, P. P. Friedmann, K. G. Powell, Hypersonic Aerothermoelastic Studies For Resuable Launch Vehicles, 45th AIAA/ASME/ASCE/AHS/ASC structures, structural dynamics & Material Converence, 19-22 April 2004, Palm Springs, California.
[9] C.I. Hung, C.K. Chen, Z.Y. Lee, Thermoelastic transient response of multilayered hollow cylinder with initial interface pressure, J. of Thermal Stresses 24(10) (2001) 987-1006.
[10] F. Armero, D. Ehrlich, Numerical modeling of softening hinges in thin Euler-Bernoulli beams, Comput. Struct. 84 (2006) 641-656.
[11] J. Dujc, B. Brank, A. Ibrahimbegovic, Multi-scale computational model for failure analysis of metal frames that includes softening and local buckling, Comput. Methods Appl. Mech. Engrg. 199 (2010) 1371-1385.
[12] A. Caggiano, G. Etse, Coupled thermo-mechanical interface model for concrete failure analysis under high temperature. Comput. Methods Appl. Mech. Engrg., 289 (2015) 498-516.
[13] A. Javili, A. McBride, P. Steinmann, Numerical modelling of thermomechanical solids with mechanically energetic (generalised) Kapitza interfaces, Computational Materials Science, 65 (2012) 542-551.
[14] W.N. E, P. Palffy-Muhoray, Dynamics of filaments during the isotropic-smectic A phase transition, J. Nonlin. Sci., 9 (1999) 417-437.
[15] A. Samanta, M.E. Tuckerman, T.Q. Yu, W.N. E, Microscopic mechanism of equilibrium melting of a solid, Science, 346(6210) (2014) 729-732.
[16] H. T. Fan, Thermal Structures Analysis and Applications of High speed Vehicles, National Defense Industry Press (in Chinese), Beijing, 2009.
[17] G. Hou, J. Wang, A. Layton, Numerical methods for fluid-structure interaction – A review, Commun. Comput. Phys., 12 (2012) 337-377.
[18] Y. C. Fung, P. Tong. Classical and Computational Solid Mechanics, World Scientific Pub. Co. Inc., 2001.
[19] D. S. Chandrasekharalah, Thermo elasticity with second sound: A review, Appl. Mech. Rev. 39 (3) (1986) 355-376.
[20] K. Hashiguchi, General description of elastoplastic deformation/sliding phenomena of solids in high accuracy and numerical efficiency: subloading surface concept, Arch. Comput. Methods Eng., 20 (2013) 361-417.
[21] F. Verdugo, N. Parés, P. Díez, Error Assessment in Structural Transient Dynamics, Arch. Comput. Methods Eng. 21 (2014) 59-90.
[22] H.W. Lord, Y. Shulman, A generalized dynamical theory of thermoelasticity, J. Mech. Phys. Solids 15 (1967) 299-309.
[23] A.E. Green, K. E. Lindsay, Thermoelasticity, Elasticity 2 (1972) 1-7.
[24] R. B. Hetnarski, M. R. Eslami, Thermal Stress – Advanced Theory and Applications, Springer 2009.
[25] W. Nowacki, Thermoelasticity: 2nd Edition, Pergamon Press 1896.
[26] J. P. Carter and J. R. Booker, Finite element analysis of coupled thermoelasticity, Comput. Struct. 31 (1) (1989) 73-80.
[27] J. H. Prevost and D. Tao, Finite element analysis of dynamic coupled thermoelasticity prob-

https://doi.org/10.4208/cicp.270515.010216a Published online by Cambridge University Press

lems with relaxation time, ASME, J. Appl. Mech. 50 (1983) 817-822.
[28] H. H. Sherief and M. N. Anwar, A problem in generalized thermoelasticity for an infinitely long annular cylinder composed of two different materials, J. Thermal Stresses 12 (1989) 529-543.
[29] Y. C. Yang, C. K. Chen, Thermoelastic transient response of an infinitely long annular cylinder composed of two different materials, Int. J. Eng. Sci. 24 (1986) 569-581.
[30] F. Osamah, F. Abdulateef, Investigation of thermal stress distribution in laser spot welding process, Al-Khwarizmi Eng. J. 5 (1) (2009) 33-41.
[31] R. Akbari Alashti, M. Khorsand, M.H. Tarahhomi, Asymmetric thermo-elastic analysis of long cylindrical shells of functionally graded materials by differential quadrature method, Proc. Inst. Mech. Eng. Part C: J. Mech. Engg. Sci. 226 (5) (2012) 1133-1147.
[32] A. Ženíšek, Finite element methods for coupled thermoelasticity and coupled consolidation of clay. RA. IRO Analyse numerique 18 (2) (1984) 183-205.
[33] S. M. Hosseini, Coupled thermoelasticity and second sound in finite length functionally graded thick hollow cylinders (without energy dissipation), Mater. Design 30 (2009) 2011-2023.
[34] D.V. Strunin, R.V.N. Melnik, A.J. Roberts, Coupled thermomechanical waves in hyperbolic thermoelasticity, J. Thermal Stresses 24 (2001) 121-140.
[35] A. Ibrahim, A. Abbas, H.M. Youssef, A nonlinear generalized thermoelasticity model of temperature-dependent materials using finite element method, Int. J. Thermophys. 33 (2012) 1302-1313.
[36] E. Serra, M. Bonaldi, A finite element formulation for thermoelastic damping analysis, Int. J. Num. Methods. Eng. 78 (6) (2009) 671-691.
[37] J. D. Lutz, D. H. Alien, W. E. Haisler, Finite-element model for the thermoelastic analysis of large composite space structures, J. Spacecraft 24 (5) (1986) 430-436.
[38] Z.H. Li, H.X. Zhang, Study on gas kinetic unified algorithm for flows from rarefied transition to continuum, J. Comput. Phys. 193 (2004) 708-738.
[39] Z.H. Li, H.X. Zhang, Gas-kinetic numerical studies of three-dimensional complex flows on spacecraft re-entry, J. Comput. Phys. 228 (2009) 1116-1138.
[40] Z.H. Li, L. Bi, H.X. Zhang, L. Li, Gas-kinetic numerical study of complex flow problems covering various flow regimes, Computers and Mathematics with Application, 61 (12) (2011) 3653-3667.
[41] Z.H. Li, J.L. Wu, X.Y. Jiang, H.X. Zhang, The unified algorithm for various flow regimes solving Boltzmann model equation in rotational non-equilibrium,Acta Aerodynamica Sinica 32(2) (2014) 137-145.
[42] Z.H. Li, A.P. Peng, H.X. Zhang, J.Y. Yang, Rarefied gas flow simulations using high-order sas-kinetic unified algorithms for Boltzmann model equations, Progress in Aerospace Sciences, 74(2015) 81-113.
[43] R.W. Lewis, P. Nithiarasu and K. N. Seetharamu, Fundamentals of the Finite Element Method for Heat and Fluid flow, John Wiley & Sons. Ltd, England, 2004.
[44] O.C. Zienkiewicz and R.L. Taylor and J.Z. Zhu, The Finite Element Method: Its Basis and fundamentals. Elsevier, 6th edition, 2005.
[45] O.C. Zienkiewicz and R.L. Taylor, The Finite Element Method For Solid and Structural Mechanics, Elsevier, 6th edition, 2005.
[46] M. G. Larson, F. Bengzon, The Finite Element Method: Theory, Implementation, and Applications, Springer, 2013.
[47] J. Frischkorn, S. Reese, Solid-beam finite element analysis of Nitinol stents, Comput. Meth-

https://doi.org/10.4208/cicp.270515.010216a Published online by Cambridge University Press

ods Appl. Mech. Engrg. 291 (2015) 42-63.
[48] W. J. T. Daniel, The subcycled Newmark algorithm, Computational Mechanics 20(3) (1997) 272-281.
[49] Z.Z. Sun, The numerical methods for partial equations, Science Press, Beijing, China, 2005 (in Chinese).
[50] L.J. Song, Y.J. Wu, A modified Crank-Nicolson scheme with incremental unknowns for convection dominated diffusion equations, Applied Mathematics and Computation, 215(9) (2010) 3293-3301.
[51] W. Gu, P. Wang, A Crank-Nicolson difference scheme for solving a type of variable coefficient delay partial differential equations, Journal of Applied Mathematics, 2(2014) 1-6.
[52] Z.H. Li, Z.Y. Wu, DSMC simulation of hypersonic rarefied flow past Apollo-CM, Acta Aerodynamic Sinica 14 (2) (1996) 230-233.
[53] J.C. Huang, K. Xu, P.B. Yu, A unified gas-kinetic scheme for continuum and rarefied flows II: multi-dimensional cases, Commun. Comput. Phys. 12(3) (2012) 662-690.
[54] H.Y. Li, Z.H. Li, W.Q. Luo, M. Li, Application and numerical method of chemical non-equilibrium flow for Teflon ablative flow fields in near-space flying condition, Sci. Sin.-Phys. Mech. Astron. 44(2) (2014) 194-202.

https://doi.org/10.4208/cicp.270515.010216a Published online by Cambridge University Press